

MOLECULAR LINE OBSERVATIONS OF INFRARED DARK CLOUDS: SEEKING THE PRECURSORS TO INTERMEDIATE AND MASSIVE STAR FORMATION

S. E. RAGAN,¹ E. A. BERGIN,¹ R. PLUME,² D. L. GIBSON,² D. J. WILNER,³ S. O'BRIEN,⁴ AND E. HAILS⁵

Received 2006 March 25; accepted 2006 June 6

ABSTRACT

We have identified 41 infrared dark clouds from the 8 μm maps of the *Midcourse Space Experiment (MSX)*, selected to be found within 1 deg^2 areas centered on known ultracompact H II regions. We have mapped these infrared dark clouds in $\text{N}_2\text{H}^+ 1\rightarrow 0$, $\text{CS } 2\rightarrow 1$, and $\text{C}^{18}\text{O } 1\rightarrow 0$ emission using the Five College Radio Astronomy Observatory. The maps of the different species often show striking differences in morphologies, indicating differences in evolutionary state and/or the presence of undetected, deeply embedded protostars. We derive an average mass for these clouds using N_2H^+ column densities of $\approx 2500 M_\odot$, a value comparable to that found in previous studies of high-mass star-forming cores using other mass tracers. The line widths of these clouds are typically $\sim 2.0\text{--}2.9 \text{ km s}^{-1}$. Based on the fact that they are dark at 8 μm , compact, and massive, and have large velocity dispersions, we suggest that these clouds may be the precursor sites of intermediate- and high-mass star formation.

Subject headings: ISM: clouds — ISM: molecules — stars: formation

Online material: machine-readable tables

1. INTRODUCTION

The study of star formation has made tremendous strides over the past two decades. Advances in observational capabilities have allowed a number of phases of the star formation process to be identified and characterized, starting with the centrally concentrated core of molecular gas that collapses to form a star surrounded by a protoplanetary disk. It has been the isolation of such objects that have not yet formed stars—prestellar cores—that has allowed us to probe the earliest initial stages of star formation (see André et al. 2000; Alves et al. 2001). Most of the progress has focused on the formation of low-mass stars, predominantly because these objects can form isolated from other nearby stars that reduces confusion, and, conveniently, there is a large sample of such objects located in nearby clouds. However, it has now been recognized that most stars that are more massive than the Sun do not form in isolated fashion, but rather in clusters of >100 stars (Zinnecker et al. 1993).

Progress in our understanding of high-mass star formation has been hampered by a number of factors: (1) timescales for massive star formation are short and examples in a given state are intrinsically rare, (2) the large distances to the giant molecular clouds (GMCs) that are the birth sites of massive stars make studies of individual objects difficult, and (3) the very nature of clustered star formation increases confusion (cf. Garay & Lizano 1999). As a result, the objects in the earliest phases—the “prestellar massive cores”—have been difficult to identify.

The traditional method of locating low-mass cores has been to examine optical plates for regions of obscured starlight and then to pursue follow-up molecular line observations (Myers & Benson 1983; Lee & Myers 1999). A comparison with the *IRAS* point source catalog then denotes whether these cores are associated with newly formed stars (Beichman et al. 1986). This

method cannot be applied to massive star-forming regions since the greater distances makes isolating individual objects difficult. Moreover, the size and high column densities of GMCs makes it impossible to use optical plates to find individual objects. An analogous method of searching for molecular cores is to search for obscured regions in Galactic mid-infrared background. However, due to atmospheric constraints, ground-based observations in the mid-IR are difficult to obtain. The *ISOCAM* instrument on the *Infrared Space Observatory* was used in this fashion, but only with pointed observations toward previously identified cores (e.g., Bacmann et al. 2000).

The *Midcourse Space Experiment (MSX)* surveyed the Galactic plane in mid-infrared bands spanning from 7 to 25 μm . This survey revealed a large population of dark clouds, predominantly located toward the inner Galaxy (Egan et al. 1998). Follow-up molecular studies of a few objects confirmed that the obscured regions represent a new population of dense, $n(\text{H}_2) > 10^5 \text{ cm}^{-3}$, and cold, $T < 20 \text{ K}$, molecular clouds (Carey et al. 1998). Further comparison to *IRAS* images demonstrated that most of these clouds are dark from 7 to 100 μm , presumably because these objects either do not contain newly formed stars, or any newly formed stars are very deeply embedded. As such, a subsample of these objects may trace massive prestellar cores. There has been substantial activity in this field recently, with numerous groups analyzing various samples of infrared dark clouds (IRDCs). These studies have shown that it is likely that IRDCs are the birth sites of high-mass stars and stellar clusters (Sridharan et al. 2005; Menten et al. 2005; Rathborne et al. 2006; Pillai et al. 2006).

We have identified a sample of infrared dark clouds and searched them for emission from the $\text{N}_2\text{H}^+ 1\rightarrow 0$, $\text{CS } 2\rightarrow 1$, and $\text{C}^{18}\text{O } 1\rightarrow 0$ transitions (§ 2). In most cases, we find that the emission closely corresponds to the *MSX* dark regions. Using a gas temperature of $T = 15 \text{ K}$ based on $\text{CO } 1\rightarrow 0$ data, we deduce several properties of the dark clouds including column density and mass (§ 3). We then summarize our findings and the implications (§ 4).

2. SOURCE SELECTION AND OBSERVATIONS

To search for prestellar massive cores we have compiled a catalog of *MSX* dark clouds. This catalog is biased, as we have

¹ Department of Astronomy, 500 Church Street, University of Michigan, Ann Arbor, MI 48109.

² Department of Physics and Astronomy, University of Calgary, Calgary, AB, Canada.

³ Harvard-Smithsonian Center for Astrophysics, Cambridge, MA.

⁴ Department of Physics, University of Notre Dame, Notre Dame, IN.

⁵ Arizona Radio Observatory, Tucson, AZ.

TABLE 1
BASIC PROPERTIES OF THE TARGET *MSX* PRE-STELLAR CORES

H II REGION	NAME	GALACTIC COORDINATES		POSITION		MAJOR AXIS (arcmin)	MINOR AXIS (arcmin)	BRIGHTNESS CONTRAST	BANDWIDTH ^a (km s ⁻¹)
		<i>l</i> (deg)	<i>b</i> (deg)	α (J2000.0)	δ (J2000.0)				
G0589.....	G5.85-0.23	5.854	-0.231	17 59 49.50	-24 00 50.25	0.64	0.60	0.409	-20-112
	G6.01-0.38	6.013	-0.384	18 00 45.13	-23 57 07.10	1.90	0.78	0.427	...
	G6.26-0.51	6.263	-0.511	18 01 46.57	-23 47 51.61	1.38	0.93	0.587	-25-107
G0867.....	G8.56+0.42	8.559	0.415	18 03 11.72	-21 20 37.48	0.40	0.36	0.286	...
	G8.64-0.09	8.636	-0.086	18 05 13.98	-21 31 21.58	0.60	0.35	0.292	...
	G9.16+0.06	9.156	0.060	18 05 46.71	-20 59 51.77	0.80	0.46	0.340	-25-107
	G9.20-0.20	9.204	-0.199	18 06 50.86	-21 04 56.00	0.80	0.47	0.288	...
	G9.21-0.22	9.213	-0.217	18 06 56.03	-21 04 59.32	0.80	0.60	0.313	-35-113
	G9.28-0.15	9.281	-0.152	18 06 49.96	-20 59 31.46	1.60	0.64	0.431	-38-116
	G9.64+0.18	9.626	0.184	18 06 17.86	-20 31 37.28	0.23	0.15	0.120	...
G1030.....	G9.80-0.15	9.796	-0.151	18 07 54.07	-20 32 30.17	0.90	0.68	0.242	...
	G9.85-0.14	9.846	-0.139	18 07 57.60	-20 29 31.81	1.20	0.80	0.254	...
	G9.86-0.04	9.856	-0.039	18 07 36.47	-20 26 05.34	1.24	0.61	0.371	-35-113
	G9.88-0.11	9.881	-0.111	18 07 55.69	-20 26 52.74	1.10	0.91	0.403	-35-113
	G10.27+0.19	10.274	0.186	18 07 38.17	-19 57 36.60	0.56	0.53	0.183	...
	G10.59-0.31	10.588	-0.311	18 10 08.02	-19 55 34.98	1.00	0.48	0.295	-35-113
	G10.70-0.33	10.704	-0.325	18 10 25.44	-19 49 53.70	1.00	0.84	0.367	-60-86
	G10.74-0.13	10.743	-0.127	18 09 46.03	-19 42 06.37	5.20	1.50	0.600	...
	G10.74+0.01	10.743	0.005	18 09 16.59	-19 38 16.41	1.23	0.93	0.413	...
	G10.99-0.09	10.989	-0.086	18 10 07.18	-19 27 59.72	0.80	0.58	0.593	-60-86
	G11.13+0.11	11.126	0.114	18 09 39.49	-19 14 59.92	0.58	0.45	0.239	...
	G11.13-0.13	11.131	-0.129	18 10 34.21	-19 21 46.84	2.40	0.60	0.463	...
	G11.23+0.07	11.226	0.068	18 10 02.01	-19 11 04.88	1.22	0.27	0.202	...
G1194.....	G11.24+0.07	11.241	0.066	18 10 04.30	-19 10 21.11	1.03	0.52	0.283	...
	G12.22+0.14	12.219	0.138	18 11 47.79	-18 16 51.43	1.68	0.80	0.388	-35-113
	G12.50-0.22	12.498	-0.222	18 13 41.44	-18 12 32.16	0.88	0.75	0.475	-35-113
	G12.58+0.27	12.578	0.273	18 12 01.49	-17 54 04.62	1.55	0.61	0.263	...
	G12.61+0.25	12.608	0.248	18 12 10.65	-17 53 13.15	0.86	0.59	0.235	...
G1504.....	G12.74-0.36	12.736	-0.361	18 14 41.01	-18 03 59.01	0.87	0.52	0.280	...
	G14.33-0.57	14.334	-0.567	18 18 37.67	-16 45 30.54	0.97	0.51	0.362	-54-93
	G14.38-0.46	14.384	-0.457	18 18 19.32	-16 39 44.47	1.36	0.76	0.268	...
	G14.40-0.60	14.398	-0.604	18 18 53.43	-16 43 10.49	1.51	1.51	0.412	...
	G14.49-0.15	14.493	-0.146	18 17 23.71	-16 25 08.20	1.68	0.90	0.465	...
	G14.64-0.57	14.636	-0.571	18 19 14.32	-16 29 39.47	2.25	0.90	0.568	...
	G14.65-0.18	14.648	-0.117	18 17 35.72	-16 16 07.42	0.70	0.32	0.346	...
	G15.05+0.09	15.053	0.089	18 17 38.41	-15 48 52.11	1.60	0.63	0.532	...
	G15.55-0.45	15.548	-0.447	18 20 34.52	-15 37 54.30	0.88	0.48	0.280	...
G1961.....	G19.25-0.07	19.246	-0.069	18 26 20.57	-12 11 16.74	0.70	0.39	0.238	...
	G19.28-0.39	19.281	-0.387	18 27 33.68	-12 18 18.35	1.08	0.78	0.417	-35-113
	G19.29+0.08	19.291	0.078	18 25 53.80	-12 04 46.57	2.75	1.10	0.447	...
	G19.35-0.04	19.348	-0.039	18 26 25.72	-12 05 01.46	0.72	0.68	0.275	...
	G19.37-0.03	19.374	-0.034	18 26 27.61	-12 03 30.32	1.01	0.80	0.375	-35-113
	G19.40-0.01	19.396	-0.006	18 26 24.05	-12 01 33.28	1.05	0.94	0.330	-35-113
	G19.91-0.21	19.913	-0.207	18 28 06.69	-11 39 42.83	1.39	0.98	0.346	...
	G19.97-0.11	19.967	-0.106	18 27 50.94	-11 34 01.67	0.65	0.65	0.275	...
G2371.....	G19.98-0.21	19.979	-0.212	18 28 15.29	-11 36 20.91	1.57	0.72	0.318	...
	G23.32+0.06	23.318	0.056	18 33 34.18	-08 31 19.32	2.10	0.42	0.259	...
	G23.37-0.29	23.368	-0.287	18 34 53.66	-08 38 08.59	0.72	0.50	0.376	37-183
	G23.38-0.13	23.378	-0.126	18 34 20.09	-08 33 09.71	0.77	0.40	0.321	...
	G23.38-0.51	23.381	-0.521	18 35 45.56	-08 43 54.76	0.71	0.60	0.227	...
	G23.38+0.29	23.383	0.288	18 32 51.52	-08 21 26.29	0.57	0.50	0.311	...
	G23.44-0.52	23.441	-0.524	18 35 52.89	-08 40 47.92	1.88	0.53	0.313	...
	G23.48+0.11	23.476	0.106	18 33 41.10	-08 21 31.62	1.22	0.54	0.378	...
	G23.48-0.53	23.481	-0.534	18 35 59.52	-08 38 56.65	1.50	0.50	0.480	-35-113
	G23.61-0.01	23.614	-0.009	18 34 21.28	-08 17 21.61	1.82	0.76	0.471	...
	G24.05-0.22	24.051	-0.216	18 35 54.61	-07 59 48.07	0.81	0.51	0.368	37-184
	G24.16+0.08	24.158	0.078	18 35 03.29	-07 45 58.96	0.90	0.84	0.390	37-184
	G24.17+0.06	24.170	0.064	18 35 07.65	-07 45 43.85	0.71	0.37	0.344	...
	G24.37-0.16	24.369	-0.157	18 36 17.34	-07 41 13.82	1.68	1.56	0.467	...
G24.37-0.21	24.371	-0.214	18 36 29.82	-07 42 41.72	2.10	0.96	0.258	...	
G24.44-0.23	24.436	-0.234	18 36 41.36	-07 39 46.99	1.54	1.51	0.546	...	
G24.63+0.15	24.629	0.148	18 35 40.73	-07 18 57.64	2.15	0.70	0.533	...	

TABLE 1—Continued

H II REGION	NAME	GALACTIC COORDINATES		POSITION		MAJOR AXIS (arcmin)	MINOR AXIS (arcmin)	BRIGHTNESS CONTRAST	BANDWIDTH ^a (km s ⁻¹)	
		<i>l</i> (deg)	<i>b</i> (deg)	α (J2000.0)	δ (J2000.0)					
G2572.....	G25.08+0.20	25.076	0.199	18 36 19.50	-06 53 44.33	0.80	0.63	0.363	...	
	G25.24-0.22	25.243	-0.216	18 38 07.16	-06 56 16.48	0.72	0.56	0.298	...	
	G25.25-0.24	25.248	-0.236	18 38 12.01	-06 56 33.53	1.00	0.50	0.283	...	
	G25.61+0.24	25.613	0.239	18 37 10.53	-06 24 01.14	1.70	1.70	0.374	...	
	G25.99-0.06	25.985	-0.057	18 38 55.26	-06 12 20.39	1.03	0.80	0.337	-35-113	
G2996.....	G30.14-0.07	30.135	-0.069	18 46 34.71	-02 31 13.90	1.40	0.60	0.287	-35-113	
	G30.31-0.28	30.309	-0.282	18 47 39.31	-02 27 46.38	0.82	0.63	0.226	...	
	G30.49-0.39	30.494	-0.392	18 48 23.10	-02 20 54.35	0.84	0.81	0.414	22-168	
	G30.53-0.27	30.353	-0.272	18 47 42.00	-02 25 08.99	1.25	0.91	0.310	-35-113	
	G30.58-0.25	30.579	-0.252	18 48 02.48	-02 12 32.12	1.53	0.58	0.305	...	
	G30.66+0.05	30.663	0.046	18 47 08.00	-01 59 53.60	1.82	0.80	0.358	...	
	G30.69+0.06	30.689	0.056	18 47 08.72	-01 58 13.85	0.75	0.63	0.217	...	
	G30.89+0.14	30.894	0.136	18 47 14.08	-01 45 05.75	1.60	0.60	0.321	-35-113	
G3141.....	G30.98-0.15	30.978	-0.148	18 48 23.97	-01 48 23.07	1.33	0.80	0.411	-35-113	
	G31.02-0.12	31.024	-0.116	18 48 22.17	-01 45 03.19	1.62	0.70	0.450	-35-113	
	G31.23+0.02	31.226	0.024	18 50 03.85	-00 37 02.40	1.20	0.80	0.361	...	
	G31.39+0.30	31.391	0.296	18 47 34.34	-01 14 10.89	2.10	1.70	0.349	...	
	G31.70-0.50	31.699	-0.496	18 50 57.27	-01 19 24.42	0.68	0.50	0.348	...	
	G31.71-0.49	31.723	-0.486	18 50 57.76	-01 17 51.09	0.63	0.60	0.336	...	
	G32.01+0.05	32.013	0.056	18 49 33.70	-00 47 32.25	1.17	1.10	0.526	-35-113	
	G32.84-0.03	32.843	-0.032	18 51 23.35	-00 05 37.42	1.30	0.97	0.357	...	
G3350.....	G33.36-0.01	33.363	-0.007	18 52 14.91	00 22 49.67	1.58	0.84	0.288	...	
	G33.42+0.13	33.418	0.126	18 51 52.52	00 29 24.18	0.44	0.25	0.217	...	
	G33.70-0.02	33.699	-0.016	18 52 53.60	00 40 31.43	1.80	0.50	0.250	...	
	G33.82-0.22	33.819	-0.219	18 53 50.10	00 41 22.54	0.90	0.53	0.432	2-149	
G3426.....	G34.13+0.08	34.134	0.076	18 53 21.57	01 06 16.14	1.68	0.50	0.254	...	
	G34.26+0.19	34.263	0.189	18 53 11.55	01 16 14.93	1.75	0.61	0.271	...	
	G34.74-0.12	34.739	-0.122	18 55 10.11	01 33 09.25	0.90	0.80	0.393	-15-131	
	G34.74+0.01	34.744	0.006	18 54 43.32	01 36 55.46	0.75	0.57	0.212	...	
	G35.04-0.47	35.043	-0.474	18 56 58.62	01 39 44.74	0.65	0.41	0.312	...	
	G3520.....	G34.63-1.03	34.627	-1.026	18 58 10.95	01 02 25.33	0.26	0.18	0.447	-29-117
		G34.78-0.80	34.778	-0.804	18 57 40.08	01 16 33.76	0.56	0.45	0.341	-35-114
G35.02-1.50		35.018	-1.497	19 00 34.38	01 10 23.16	0.97	0.35	0.375	...	
G35.20-0.72		35.203	-0.721	18 58 08.92	01 41 31.31	0.78	0.51	0.436	-29-117	
G3755.....	G37.08-0.15	37.081	-0.149	18 59 32.80	03 37 25.91	0.42	0.50	0.321	...	
	G37.25+0.01	37.253	0.011	18 59 17.48	03 50 59.94	0.98	0.52	0.296	...	
	G37.42+0.17	37.418	0.173	18 59 00.95	04 04 14.78	0.70	0.64	0.342	...	
	G37.44+0.14	37.439	0.138	18 59 10.75	04 04 24.37	0.79	0.40	0.322	-35-113	
	G37.89-0.15	37.886	-0.152	19 01 02.00	04 20 18.23	1.03	0.58	0.325	-26-107	
G4318.....	G43.19-0.16	43.187	-0.162	19 10 53.01	09 02 30.58	0.42	0.20	0.304	...	
	G43.32-0.20	43.318	-0.204	19 11 16.78	09 08 18.83	0.50	0.42	0.165	...	
	G43.78+0.05	43.776	0.046	19 11 14.38	09 39 36.89	0.92	0.91	0.377	-23-124	
G4389.....	G43.64-0.82	43.644	-0.824	19 14 07.05	09 08 24.64	0.60	0.21	0.577	-19-127	
G4426.....	G44.29-0.09	44.291	-0.092	19 12 42.25	10 03 10.40	0.71	0.46	0.219	...	
G5023.....	G48.84+0.15	48.836	0.151	19 20 29.90	14 11 12.12	1.22	0.58	0.317	...	
	G48.84+0.14	48.848	0.136	19 20 34.57	14 11 24.84	0.70	0.43	0.242	...	
	G50.07+0.06	50.071	0.059	19 23 14.36	15 13 58.11	0.86	0.33	0.378	-13-133	
G5031.....	G51.00-0.18	51.001	-0.177	19 22 55.92	15 56 24.24	0.60	0.35	0.290	...	
G5410.....	G53.88-0.18	53.879	-0.181	19 31 42.73	18 27 55.78	1.12	0.42	0.417	-30-116	
G6148.....	G61.52+0.02	61.519	0.024	19 47 09.72	25 13 00.46	0.60	0.45	0.334	...	
G7578.....	G75.75+0.75	75.753	0.749	20 19 57.75	37 39 01.90	1.10	0.90	0.474	-33-113	
	G76.38+0.63	76.381	0.626	20 22 17.04	38 05 50.23	0.40	0.30	0.318	-33-113	

NOTE.—Units of right ascension are hours, minutes, and seconds, and units of declination are degrees, arcminutes, and arcseconds. Table 1 is also available in machine-readable form in the electronic edition of the *Astrophysical Journal Supplement*.

^a For observed regions, we give the total velocity range to which the observations were sensitive. A given object was probed in the same velocity range for each observed transition.

only searched the released MSX band A (centered at 8.8 μm) images for infrared dark clouds in the vicinity of known ultra-compact (UC) H II regions from the Wood & Churchwell (1989) catalog. More specifically, we searched for absorbing clouds within a square degree centered on a given UC H II region. This strategy takes advantage of the fact that young stars generally

form in clusters, and, therefore, a good place to search for the precursors to massive stars is in the vicinity of regions with current massive star formation evidenced by the UC H II regions. In this fashion we have isolated 114 infrared dark clouds, of which only a small fraction (15%) have known associations with radio sources or masers. From this catalog of 114 infrared dark

clouds we selected a subsample of the 41 most compact and most opaque ($\tau_{8.8 \mu\text{m}} \gtrsim 0.4$) cores and targeted these for molecular line observations.

We mapped 41 of the sample of *MSX* dark clouds in emission from $\text{C}^{18}\text{O } J = 1 \rightarrow 0$ ($\nu = 109.782$ GHz), $\text{CS } J = 2 \rightarrow 1$ ($\nu = 97.981$ GHz), and $\text{N}_2\text{H}^+ J = 1 \rightarrow 0$ ($\nu = 93.173$ GHz) using the 14 m Five College Radio Astronomy Observatory (FCRAO). The observations were made in 2002 February, May, and December using the 16 element focal plane array receiver SEQUOIA. Each 2.5×2.5 region was mapped with the $50''$ beam, with typical rms noise levels of ~ 0.05 – 0.1 K. We used the Narrow Band Correlator configured to a velocity resolution of ~ 0.13 km s $^{-1}$. Typical system temperatures (T_{sys}) were 200–300 K. Main beam efficiencies (η_{mb}) were approximated at 50% from the standard FCRAO values. This is accurate within a few percent for each transition. For each spectrum, a first-order, linear baseline was fitted to remove instrumental and continuum offsets and drift.

This selection of species is motivated by studies of low-mass prestellar clouds. N_2H^+ is unlikely to significantly suffer from the effects of depletion as the core condenses, and this species is a good tracer of the dense centers of starless cores (Bergin & Langer 1997; Tafalla et al. 2002). Conversely, C^{18}O and CS emission can be used to trace the outer layers. Table 1 lists some basic dark cloud properties such as the H II region name, the coordinates, the size, and the center-to-edge brightness contrast. The brightness contrast was obtained by comparing the brightness in the band centered at $8.8 \mu\text{m}$ at the center of the core with the average background brightness, estimated from an average of the intensities in a vertical and horizontal slit across the dark region. If the dark cloud was searched for molecular emission, we provide the LSR velocity range to which the observations were sensitive.

In an Appendix, we provide a source by source description of any associations with known star formation indicators (e.g., *IRAS* sources, masers, radio continuum sources). The large majority of our sources have no association with any known strong infrared source.

3. RESULTS

3.1. Molecular Line Fits

Each line is fitted with a Gaussian profile to determine the integrated intensity, line width, and the LSR velocity of the emitting material. Table 2 presents the results of the spectral line fitting. All parameters were extracted by standard Gaussian fitting methods in the CLASS package (Buisson et al. 2002); for N_2H^+ , the seven main hyperfine components were fitted together using the HFS routine. The reported line-center velocity corresponds to that of the strongest hyperfine component ($J = 1 \rightarrow 0$, F_1 , $F = 2, 3 \rightarrow 1, 2$) at 93.1738 GHz.

Our observations were obtained with velocity resolution of 0.13 km s $^{-1}$, and to increase the signal to noise, we on occasion smoothed the line profiles by a factor of 2. As such, we had little sensitivity to structure within the line. Within our sensitivity limits (see § 2), we see no evidence for extended line wings, and all lines were well fitted by single Gaussians. We report here only basic line properties.

3.2. Molecular Emission Morphologies

Figure 1 displays the *MSX* images of each dark cloud overlaid with the integrated intensity maps of molecular emission for all observed molecular transitions. The contour levels for each dark cloud are specified in the captions. In some cases, multiple velocity components are detected, and the different velocity components

are given different colors. The blue contours always correspond to the molecular emission morphology that most closely corresponds to the distribution of $8 \mu\text{m}$ absorption seen in the *MSX* image and, therefore, is most likely to be associated with the dark cloud. The line properties of the other velocity components (i.e., emission that is unassociated with the absorbing cloud) are not reported. There are three cases in which an a/b designation was assigned to distinguish two emission peaks. For G14.33–0.57 and G23.48–0.53, there are two spatially distinct and separate emission peaks at approximately the same characteristic velocity. This may suggest that in these cases, we were able to resolve spatially separated fragments of a cloud. In the case of G37.44+0.14, there are two velocity components that appear to correspond to absorbing regions (the 40 km s $^{-1}$ feature corresponding to the central absorbing cloud; the 18 km s $^{-1}$ feature corresponding to absorption to the north and west). Based on our assumptions, this would indicate that there are two unassociated dark clouds apparent in the same region of the sky by chance.

The morphological differences seen in Figure 1 are striking. Some maps show well defined cores in all three molecular tracers (e.g., G32.01+0.05). Other maps, like G06.26–0.51, show fairly well defined cores in C^{18}O and CS, but nothing obvious is seen in the N_2H^+ . And others, like G09.21–0.22, show a strong centrally concentrated N_2H^+ core but CS that is much more diffuse. Finally, there are cores like G10.59–0.31 that show no real evidence for molecular emission centered on the dark cloud at all. In this case, it is possible that any molecular emission directly associated with the dark cloud lies outside of the observed velocity band (see Table 1).

These differences in the molecular emission maps may be the result of differences in the evolutionary states. It is well known that CS and C^{18}O can form relatively quickly in the gas phase, whereas N_2H^+ takes significantly longer. However, as density enhances, the CS and C^{18}O tend to deplete onto the surfaces of dust grains, whereas N_2H^+ will remain in the gas phase. On protostar formation, CS and C^{18}O can be released from dust grain surfaces (e.g., see models of Bergin & Langer 1997; Lee et al. 2004). Therefore, two scenarios can lead to the low abundance of N_2H^+ relative to CS or C^{18}O : the star-forming core is at an early stage of condensation and the densities are low such that CS and C^{18}O would be not affected by dust depletion, or the presence of a protostar has released the CS and C^{18}O from dust grains, all the while the N_2H^+ abundance is essentially unchanged throughout the process. Another possible explanation of the differences seen in the maps is that some of the dark clouds may contain as yet undetected protostars, obscured by the high opacity apparent in the $8.8 \mu\text{m}$ *MSX* images. If a protostar is present, it can alter the local gas chemistry via grain mantle evaporation, which can change the emission morphologies (Jørgensen 2004). We are using data from the *Spitzer Space Telescope* to determine which dark clouds are truly starless and which contain embedded protostars in a subsample of these objects (S. E. Ragan et al. 2006, in preparation).

3.3. Distance Estimates

The kinematic distance to each dark cloud is calculated using the line center velocity and the Milky Way rotation curve model of Fich et al. (1989). The distance assignments are presented in Table 3 for dark clouds for which we estimated masses. (Sources to which we are unable to assign a distance or those that show no significant emission are not subject to further calculations.) For every position, there is both a “near” and “far” distance solution that corresponds to the characteristic velocity of the emission. In

TABLE 2
MOLECULAR LINE OBSERVATIONS

SOURCE	$\text{N}_2\text{H}^+ J = 1-0$			$\text{C}^{18}\text{O } J = 1-0$			$\text{CS } J = 2-1$				
	$\Delta\alpha$ (arcmin)	$\Delta\delta$ (arcmin)	$\int T_A^* dv$ (K km s $^{-1}$)	V (km s $^{-1}$)	Δv (km s $^{-1}$)	$\int T_A^* dv$ (K km s $^{-1}$)	V (km s $^{-1}$)	Δv (km s $^{-1}$)	$\int T_A^* dv$ (K km s $^{-1}$)	V (km s $^{-1}$)	Δv (km s $^{-1}$)
G05.85-0.23.....	0.4	-0.4	1.21 (0.15)	17.2 (0.1)	0.8 (0.1)	1.44 (0.17)	17.0 (0.1)	1.7 (0.2)	0.47 (0.10)	16.9 (0.2)	2.2 (0.3)
G06.26-0.51.....	0.0	0.0	(<0.15)	1.69 (0.11)	22.7 (0.1)	2.3 (0.2)	1.64 (0.15)	23.2 (0.2)	4.2 (0.5)
G09.16+0.06.....	0.0	0.0	(<0.12)	1.39 (0.09)	31.3 (0.1)	1.7 (0.1)	0.40 (0.07)	31.3 (0.1)	1.2 (0.3)
G09.21-0.22.....	0.0	0.0	3.59 (0.15)	42.8 (0.1)	1.8 (0.2)	1.29 (0.11)	42.7 (0.1)	2.8 (0.3)
G09.28-0.15.....	0.0	0.0	3.66 (0.10)	41.4 (0.1)	1.9 (0.4)	1.27 (0.12)	41.3 (0.1)	2.6 (0.3)
G09.86-0.04.....	0.0	0.0	0.87 (0.11)	18.1 (0.1)	1.1 (0.2)	1.52 (0.14)	17.8 (0.1)	2.3 (0.2)
G09.88-0.11.....	0.0	0.0	(<0.13)	0.54 (0.15)	17.3 (0.2)	1.8 (0.6)
G10.59-0.31.....	0.0	0.0	(<0.40)	(<0.24)
G10.70-0.33.....	0.0	0.0	(<0.13)	(<0.13)
G10.99-0.09.....	0.0	0.0	4.24 (0.11)	29.6 (0.1)	2.4 (0.2)	2.25 (0.17)	29.5 (0.1)	2.2 (0.2)	1.00 (0.12)	29.2 (0.3)	4.2 (0.5)
G12.22+0.14.....	0.0	0.0	3.60 (0.08)	39.6 (0.1)	1.7 (0.1)	1.78 (0.07)	36.7 (0.1)	2.2 (0.1)
G12.50-0.22.....	0.0	0.0	2.97 (0.10)	35.8 (0.1)	1.8 (0.1)	1.60 (0.13)	35.7 (0.1)	1.8 (0.2)	1.40 (0.10)	35.6 (0.1)	2.0 (0.2)
G14.33-0.57a.....	0.0	0.0	(<0.14)	2.19 (0.15)	19.3 (0.1)	2.1 (0.2)	1.25 (0.13)	19.6 (0.1)	2.4 (0.3)
G14.33-0.57b.....	-1.7	0.8	1.42 (0.14)	20.0 (0.1)	1.1 (0.2)	1.81 (0.12)	19.9 (0.1)	1.6 (0.2)	0.84 (0.10)	20.3 (0.1)	1.4 (0.2)
G19.28-0.39.....	0.0	0.0	(<0.17)	0.26 (0.07)	54.0 (0.1)	1.1 (0.2)
G19.37-0.03.....	0.0	0.0	3.62 (0.11)	27.3 (0.1)	2.5 (0.1)	3.02 (0.07)	27.0 (0.1)	3.8 (0.1)
G19.40-0.01.....	0.0	0.0	0.95 (0.11)	27.0 (0.1)	1.2 (0.3)	0.81 (0.06)	26.5 (0.1)	2.9 (0.3)
G23.37-0.29.....	0.0	0.0	2.88 (0.27)	78.5 (0.1)	2.0 (0.2)	3.97 (0.21)	78.1 (0.1)	2.7 (0.2)	2.30 (0.12)	77.8 (0.1)	4.8 (0.3)
G23.48-0.53a.....	0.0	0.0	1.45 (0.12)	64.8 (0.1)	2.5 (0.4)	0.90 (0.09)	63.9 (0.3)	4.8 (0.6)
G23.48-0.53b.....	-2.1	-2.1	1.24 (0.12)	62.8 (0.1)	2.9 (0.4)	0.73 (0.08)	62.7 (0.3)	2.9 (0.4)
G24.05-0.22.....	0.0	0.0	2.71 (0.21)	81.4 (0.1)	1.9 (0.3)	2.30 (0.10)	81.5 (0.1)	2.0 (0.1)	1.00 (0.13)	82.0 (0.2)	2.8 (0.5)
G24.16+0.08.....	0.0	0.0	(<0.10)	1.64 (0.16)	51.8 (0.1)	1.9 (0.2)	(<0.10)
G25.99-0.06.....	0.0	0.0	0.80 (0.15)	89.9 (0.3)	1.6 (0.5)	1.05 (0.11)	90.2 (0.1)	2.4 (0.3)
G30.14-0.07.....	0.0	0.0	(<0.12)	(<0.15)	86.8 (0.2) ^a	2.7 (0.5) ^a
G30.49-0.39.....	1.2	-0.8	(<0.14)	0.62 (0.12)	106.4 (0.3)	3.0 (0.9)
G30.53-0.27.....	0.0	0.0	(<0.12)	1.73 (0.19)	102.9 (0.4)	7.3 (0.9)
G30.89+0.14.....	0.0	0.0	1.29 (0.13)	96.5 (0.2)	3.4 (0.3)	0.56 (0.10)	95.9 (0.3)	3.0 (0.5)
G30.98-0.15.....	-0.4	0.0	4.56 (0.12)	77.9 (0.1)	2.6 (0.1)	2.27 (0.11)	77.9 (0.1)	4.3 (0.2)
G31.02-0.12.....	0.0	0.0	1.57 (0.07)	76.6 (0.1)	2.2 (0.2)	1.24 (0.11)	76.2 (0.1)	3.0 (0.3)	0.66 (0.08)	76.6 (0.2)	3.3 (0.4)
G32.01+0.05.....	0.0	0.0	7.18 (0.10)	95.3 (0.1)	3.9 (0.1)	4.42 (0.12)	97.2 (0.1)	4.7 (0.2)	4.03 (0.09)	96.0 (0.1)	6.8 (0.2)
G33.82-0.22.....	0.0	0.0	1.03 (0.11)	11.3 (0.1)	1.0 (0.3)	0.48 (0.09)	11.5 (0.1)	1.0 (0.2)
G34.63-1.03.....	0.0	0.0	1.16 (0.15)	13.6 (0.2)	2.6 (0.6)	0.58 (0.08)	12.8 (0.1)	1.1 (0.2)	(<0.15)
G34.74-0.12.....	0.0	0.0	1.92 (0.17)	79.1 (0.1)	2.7 (0.3)	3.51 (0.14)	78.9 (0.2)	2.1 (0.1)	1.11 (0.10)	78.9 (0.2)	3.8 (0.4)
G34.78-0.80.....	0.0	0.0	0.33 (0.11)	43.2 (0.4)	3.0 (0.7)	2.25 (0.10)	44.1 (0.1)	3.3 (0.1)	1.83 (0.07)	43.5 (0.1)	3.0 (0.2)
G35.20-0.72.....	0.0	0.0	3.02 (0.20)	33.1 (0.1)	2.5 (0.3)	2.04 (0.12)	33.2 (0.1)	1.9 (0.1)	1.91 (0.13)	33.2 (0.1)	3.4 (0.3)
G37.44+0.14a.....	0.0	0.0	(<0.10)	1.14 (0.06)	40.0 (0.1)	1.6 (0.1)	0.77 (0.04)	40.1 (0.1)	1.4 (0.1)
G37.44+0.14b.....	-2.5	-0.4	0.65 (0.08)	17.8 (0.1)	0.5 (0.1)	0.52 (0.04)	17.8 (0.1)	0.7 (0.1)	0.25 (0.03)	17.7 (0.1)	0.9 (0.1)
G37.89-0.15.....	0.0	0.0	0.45 (0.08)	12.9 (0.1)	0.7 (0.1)	0.63 (0.04)	12.9 (0.1)	0.7 (0.1)	0.36 (0.04)	13.0 (0.1)	0.7 (0.1)
G43.64-0.82.....	0.4	2.4	(<0.25)	0.25 (0.05)	85.4 (0.1)	0.5 (0.1)
G43.78+0.05.....	0.0	0.0	(<0.17)	(<0.09)
G50.07+0.06.....	-0.8	-0.8	(<0.19)	0.73 (0.08)	54.8 (0.1)	1.5 (0.2)
G53.88-0.18.....	0.0	0.0	(<0.21)	(<0.12)
G75.75+0.75.....	0.0	0.0	(<0.12)	(<0.07)
G76.38+0.63.....	0.0	0.0	(<0.15)	(<0.07)

NOTE.—Table 2 is also available in machine-readable form in the electronic edition of the *Astrophysical Journal Supplement*.

^a Nondetection of CS in single scan. Average of 25 scans detects a weak line at the 5 σ level. The velocity and line width from this average are provided in the table.

addition to this ambiguity, Fich et al. (1989) cite a $\pm 14\%$ maximal deviation of the data from their rotation curve model; based on this consideration, we calculate errors in the distances and provide them in Table 3. In the cases where no error range (or an incomplete one) is given, no physical solution exists when calculating the distance with that error offset. For all subsequent calculations, we assume that the dark cloud is located at the “near” distance. We believe that this is a reasonable assumption since the clouds are seen in absorption against the Galactic mid-infrared background and, therefore, are unlikely to reside at the “far” distance. Assuming the “near” kinematical distance, which is also listed in Table 4, a typical core has a diameter of ~ 0.9 pc.

Interestingly, the kinematical distances for the velocity component associated with the absorption are seldom coincident with the distances estimated for the UC H II region that was the original search target. In most cases we detect molecular emission at a single velocity, and no possible distance solution from the Galactic rotation curve is consistent with the distance to the UC H II region. However, in the cases where there are multiple velocity components, the distance to the UC H II region is often consistent with one of the kinematic distance solutions for a secondary velocity component. For example, G37.44+0.14 has a secondary detection of a component at 18 km s $^{-1}$, and the “far” distance associated with it (12.34 kpc) is very close to the distance

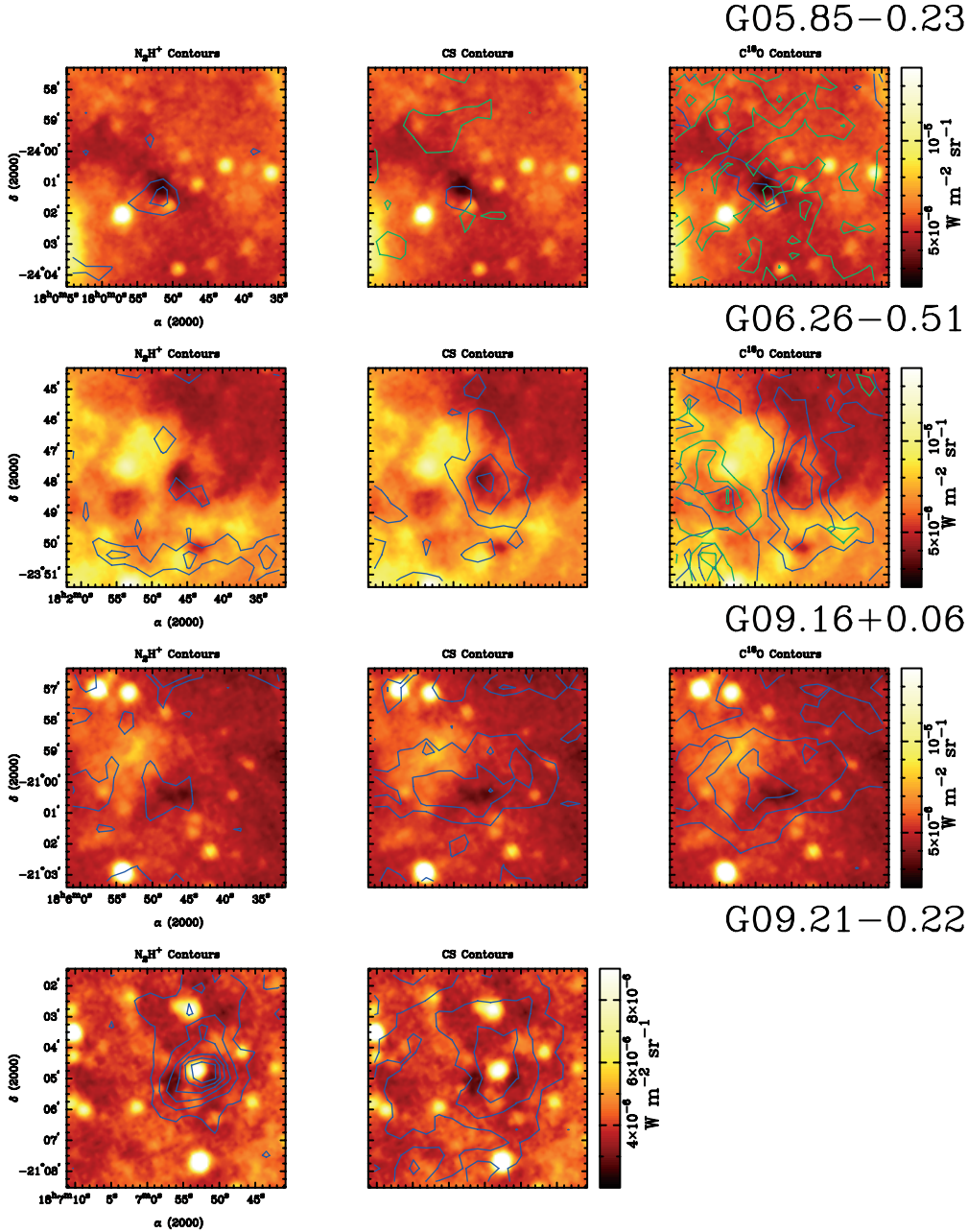
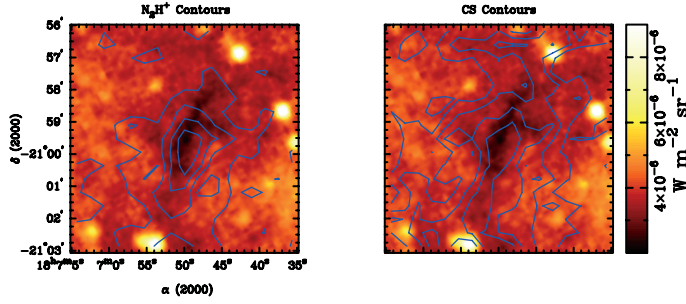
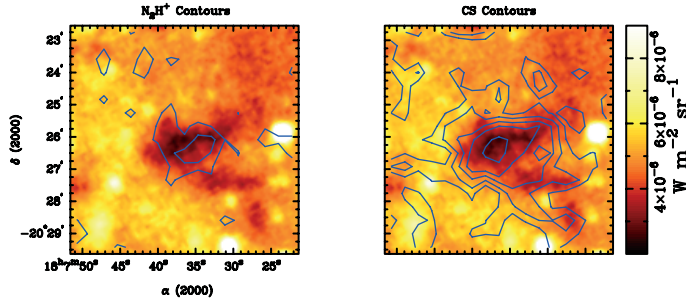


FIG. 1.—Color image shows the $8\ \mu\text{m}$ MSX, and the color bar indicates the emission intensity scale in $\text{W m}^{-2}\ \text{sr}^{-1}$. The contours represent the molecular line integrated intensity, for which the levels are listed for each object. The integrated emission was calculated within a $6\text{--}10\ \text{km s}^{-1}$ window for C^{18}O and CS. For N_2H^+ the window was $15\text{--}20\ \text{km s}^{-1}$ with some gaps accounting for the clustering of the hyperfine components. *G05.85-0.23*: blue contours show emission at $17\ \text{km s}^{-1}$; green contours: $9\ \text{km s}^{-1}$. Levels: $1.2\ \text{K km s}^{-1}$ for all plots. *G06.26-0.51*: blue contours: $23\ \text{km s}^{-1}$; green contours: $17\ \text{km s}^{-1}$. Levels: N_2H^+ : $0.5, 1\ \text{K km s}^{-1}$. CS: $1, 2, 3, 4\ \text{K km s}^{-1}$. C^{18}O : $1, 2, 3\ \text{K km s}^{-1}$ for both velocities. *G09.16+0.06*: blue contours: $31\ \text{km s}^{-1}$. Levels: N_2H^+ : $1, 2\ \text{K km s}^{-1}$. CS: $0.5, 1, 1.5\ \text{K km s}^{-1}$. C^{18}O : $1, 2, 3\ \text{K km s}^{-1}$. *G09.21-0.22*: blue contours: $43\ \text{km s}^{-1}$. Levels: N_2H^+ : $2, 4, 6, 8, 10, 12\ \text{K km s}^{-1}$. CS: $1, 2, 3\ \text{K km s}^{-1}$. *G09.28-0.15*: blue contours: $42\ \text{km s}^{-1}$. Levels: N_2H^+ : $1.5, 3, 4, 5, 6, 7, 5\ \text{K km s}^{-1}$. CS: $0.5, 1, 1.5, 2, 3\ \text{K km s}^{-1}$. *G09.88-0.11*: blue contours: $17\ \text{km s}^{-1}$. Levels: N_2H^+ : $1, 2\ \text{K km s}^{-1}$. CS: $0.5, 1, 1.5, 2, 3\ \text{K km s}^{-1}$. *G09.86-0.04*: blue contours: $18\ \text{km s}^{-1}$. Levels: N_2H^+ : $1.5, 3, 4, 5, 6, 7, 5\ \text{K km s}^{-1}$. CS: $0.5, 1, 1.5, 2, 3\ \text{K km s}^{-1}$. *G09.88-0.11*: blue contours: $17\ \text{km s}^{-1}$. Levels: N_2H^+ : $1, 2\ \text{K km s}^{-1}$. CS: $0.5, 1, 1.5, 2, 3\ \text{K km s}^{-1}$. *G10.59-0.31*: blue contours: $17\ \text{km s}^{-1}$. Levels: $3, 5, 7, 9, 11\ \text{K km s}^{-1}$ for both molecules. *G10.70-0.33*: blue contours: $0\ \text{km s}^{-1}$; green contours: $33\ \text{km s}^{-1}$. Levels: $2, 3, 4, 5\ \text{K km s}^{-1}$ for both molecules/velocities. *G10.99-0.09*: blue contours: $30\ \text{km s}^{-1}$. Levels: N_2H^+ : $2, 4, 6, 8, 10\ \text{K km s}^{-1}$. CS: $1, 1.5, 2\ \text{K km s}^{-1}$. C^{18}O : $2, 3, 4, 5\ \text{K km s}^{-1}$. *G12.22+0.14*: blue contours: $40\ \text{km s}^{-1}$. Levels: $1, 2, 3, 4, 5\ \text{K km s}^{-1}$ for each molecule. *G12.50-0.22*: blue contours: $36\ \text{km s}^{-1}$. Levels: N_2H^+ : $2, 4, 6, 8, 10\ \text{K km s}^{-1}$. CS: $1, 2, 3, 4\ \text{K km s}^{-1}$. C^{18}O : $1, 2, 3\ \text{K km s}^{-1}$. *G14.33-0.57*: blue contours: $19\ \text{km s}^{-1}$. Levels: N_2H^+ : $1, 2\ \text{K km s}^{-1}$ (solid (a)), $20\ \text{km s}^{-1}$ (dashed (b)). Levels: N_2H^+ : $2, 4, 6, 8, 10\ \text{K km s}^{-1}$. CS: $2, 3, 4, 5, 6, 7\ \text{K km s}^{-1}$. C^{18}O : $4, 5, 6, 7, 8, 9\ \text{K km s}^{-1}$ (a); $2, 3, 4\ \text{K km s}^{-1}$ (b). *G19.37-0.03*: blue contours: $27\ \text{km s}^{-1}$. Levels: N_2H^+ : $1, 3, 5, 7, 9, 11\ \text{K km s}^{-1}$. CS: $1, 2, 5, 4, 5, 5, 7\ \text{K km s}^{-1}$. *G23.37-0.29*: blue contours: $78\ \text{km s}^{-1}$; green contours: $103\ \text{km s}^{-1}$; white contours: $65\ \text{km s}^{-1}$. Levels: N_2H^+ : $3, 6, 9, 12, 15, 18\ \text{K km s}^{-1}$ ($78\ \text{km s}^{-1}$ component); $4, 6, 8, 10\ \text{K km s}^{-1}$ ($103\ \text{km s}^{-1}$). CS: $3, 4, 5, 6, 7\ \text{K km s}^{-1}$ ($78\ \text{km s}^{-1}$); $3, 4, 5, 6\ \text{K km s}^{-1}$ ($103\ \text{km s}^{-1}$); $3, 4, 5, 6, 9\ \text{K km s}^{-1}$ ($103\ \text{km s}^{-1}$). C^{18}O : $5, 7, 9, 11\ \text{K km s}^{-1}$ ($78\ \text{km s}^{-1}$); $3, 6, 9, 12, 15, 18, 21, 24\ \text{K km s}^{-1}$ ($103\ \text{km s}^{-1}$); $3, 6, 9\ \text{K km s}^{-1}$ ($65\ \text{km s}^{-1}$). *G23.48-0.53*: blue contours: $64\ \text{km s}^{-1}$; green contours: $76\ \text{km s}^{-1}$. Levels: $1, 1.5, 2, 2.5\ \text{K km s}^{-1}$ both molecules/velocities. *G24.05-0.22*: blue contours: $82\ \text{km s}^{-1}$. Levels: N_2H^+ : $1, 2, 3\ \text{K km s}^{-1}$. CS: $1, 2, 3, 4\ \text{K km s}^{-1}$. C^{18}O : $1, 2, 3, 4, 5\ \text{K km s}^{-1}$. *G24.16+0.08*: blue contours: $53\ \text{km s}^{-1}$; green contours: $113\ \text{km s}^{-1}$. Levels: N_2H^+ : $1, 2, 3\ \text{K km s}^{-1}$ ($113\ \text{km s}^{-1}$ component). CS: $1, 2, 3\ \text{K km s}^{-1}$ in both velocities. C^{18}O : $1, 2, 3\ \text{K km s}^{-1}$ ($53\ \text{km s}^{-1}$); $2, 4, 6\ \text{K km s}^{-1}$ ($113\ \text{km s}^{-1}$). *G25.99-0.06*: blue contours: $90\ \text{km s}^{-1}$. Levels: N_2H^+ : $1, 2, 3\ \text{K km s}^{-1}$. CS: $1, 2\ \text{K km s}^{-1}$. *G30.14-0.07*: blue contours:

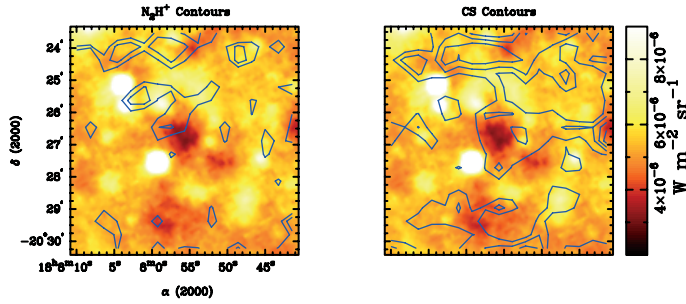
G09.28–0.15



G09.86–0.04



G09.88–0.11



G10.59–0.31

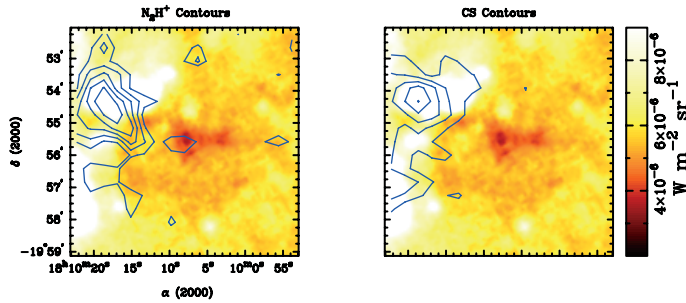


FIG. 1.—*Continued.* 87 km s⁻¹. Levels: 0.5 for both molecules. *G30.53–0.27*: blue contours : 103 km s⁻¹. Levels: N₂H⁺ : 0.5 K km s⁻¹. CS : 1,1.5,2,2.5 K km s⁻¹. *G30.89+0.14*: blue contours : 96 km s⁻¹; green contours : 40 km s⁻¹; white contours : 108 km s⁻¹. Levels: N₂H⁺ : 2,3,4 K km s⁻¹ (96 km s⁻¹ component); 2,4,6,8,10 K km s⁻¹ (40 km s⁻¹); 2,4,6,8,10 K km s⁻¹ (108 km s⁻¹). CS : 3,4,5,6,7 K km s⁻¹ (96 km s⁻¹); 2,3,4 K km s⁻¹ (40 km s⁻¹ and 108 km s⁻¹ components). *G30.98–0.15*: blue contours : 78 km s⁻¹. Levels: N₂H⁺ : 1,2,4,6,8 K km s⁻¹. CS : 1,2,3,4 K km s⁻¹. *G31.02–0.12*: blue contours : 76 km s⁻¹; green contours : 83 km s⁻¹; white contours : 92 km s⁻¹. Levels: N₂H⁺ : 1,2,3,4 K km s⁻¹ (76 km s⁻¹ and 83 km s⁻¹ components); 2,4,6,8,10 K km s⁻¹ (92 km s⁻¹). CS : 1,2,3,4,5,6,7 K km s⁻¹ (76 km s⁻¹); 1,2,3,4,5,6 K km s⁻¹ (83 km s⁻¹); 1,2,3,4,5,6,9 K km s⁻¹ (92 km s⁻¹). C¹⁸O : 1,2,3,4,5,6,7,8,9 K km s⁻¹ (76 km s⁻¹); 1,2,3,6,9,12,15,18,21,24 K km s⁻¹ (83 km s⁻¹); 1,2,3 K km s⁻¹ (92 km s⁻¹). *G32.01+0.05*: blue contours : 95 km s⁻¹. Levels: N₂H⁺ : 3,6,9,12,15,18,21,24 K km s⁻¹. CS : 2,4,6,8,10 K km s⁻¹. C¹⁸O : 2,4,6,8,10 K km s⁻¹. *G33.82–0.22*: blue contours : 11 km s⁻¹. Levels: N₂H⁺ : 1,2,3 K km s⁻¹. CS : 0.5,1 K km s⁻¹. *G34.63–1.03*: blue contours : 14 km s⁻¹. Levels: N₂H⁺ : 1,2,3 K km s⁻¹. CS : 0.5,1,0 K km s⁻¹. C¹⁸O : 0.5,1,1.5 K km s⁻¹. *G34.74–0.12*: blue contours : 79 km s⁻¹. Levels: N₂H⁺ : 1,2,3 K km s⁻¹. CS : 1,2,3,4 K km s⁻¹. C¹⁸O : 1,2,3,4,5 K km s⁻¹. *G34.78–0.80*: blue contours : 44 km s⁻¹; green contours : 37 km s⁻¹. Levels: N₂H⁺ : 1,2,3,4 K km s⁻¹ for both velocities. CS : 1,2,3 K km s⁻¹ for both velocities. C¹⁸O : 1,2,3 K km s⁻¹ (44 km s⁻¹ component); 1,2,3,4,5,6 K km s⁻¹ (37 km s⁻¹). *G35.20–0.72*: blue contours : 33 km s⁻¹. Levels: N₂H⁺ : 2,4,6,8,10,12,14 K km s⁻¹. CS : 2,4,6,8,10,12 K km s⁻¹. C¹⁸O : 2,4,6,8,10,12,14 K km s⁻¹. *G37.44+0.14*: blue contours : 40 km s⁻¹; green contours : 18 km s⁻¹; white contours : 86 km s⁻¹. Levels: 0.5,1,2,3 K km s⁻¹ for all molecules/velocities. *G37.89–0.15*: blue contours : 13 km s⁻¹; green contours : 65 km s⁻¹; white contours : 86 km s⁻¹. Levels: N₂H⁺ : 0.5,1,2,3 K km s⁻¹ (13 km s⁻¹ component). CS : 0.5,1,2,3 K km s⁻¹ (13 km s⁻¹). C¹⁸O : 0.5,1,2,3 K km s⁻¹ (13 km s⁻¹ and 65 km s⁻¹); 2,3 K km s⁻¹ (86 km s⁻¹). *G50.07+0.06*: blue contours 55 km s⁻¹. Levels: 0.5,1 K km s⁻¹ for both molecules.

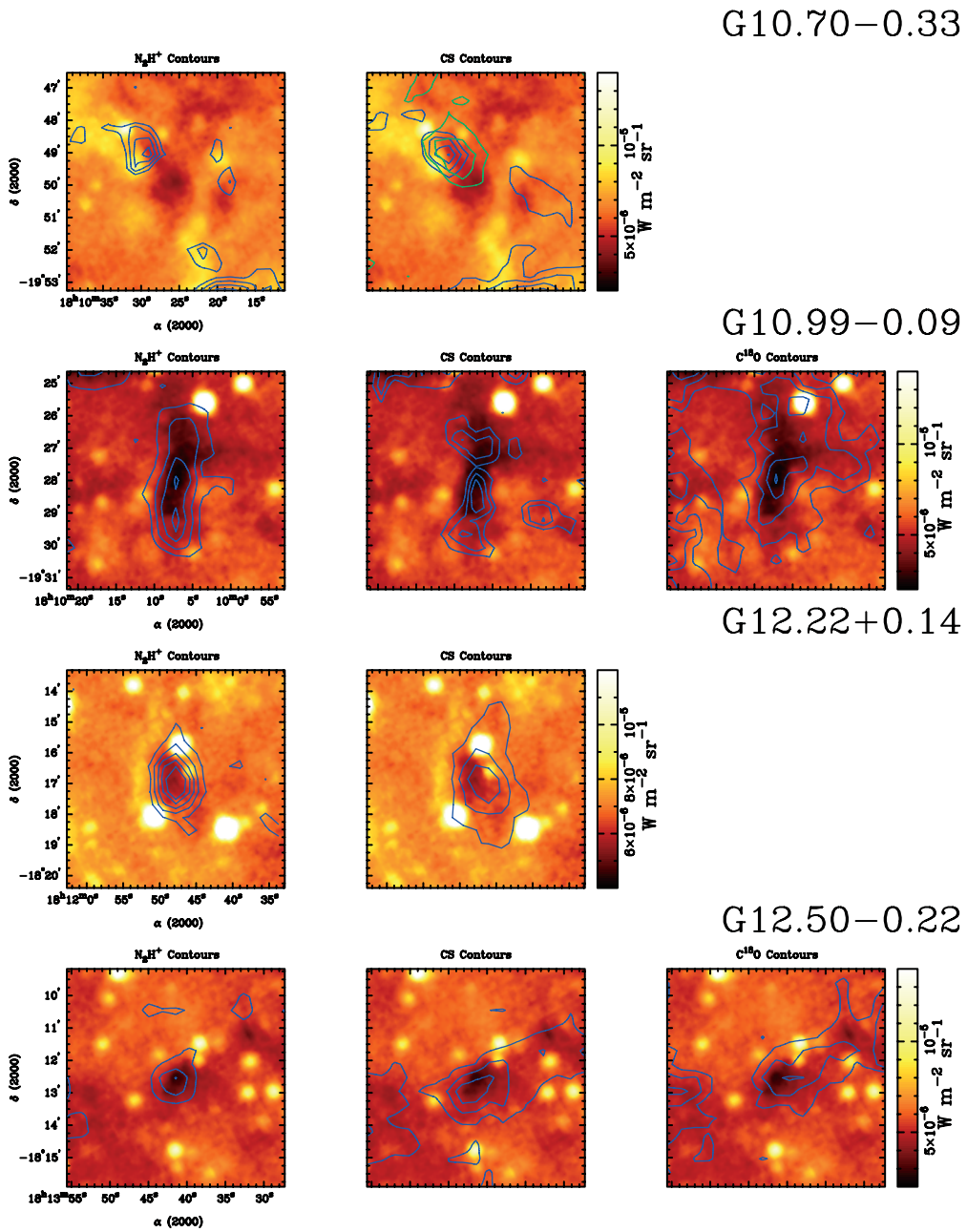


FIG. 1.— *Continued*

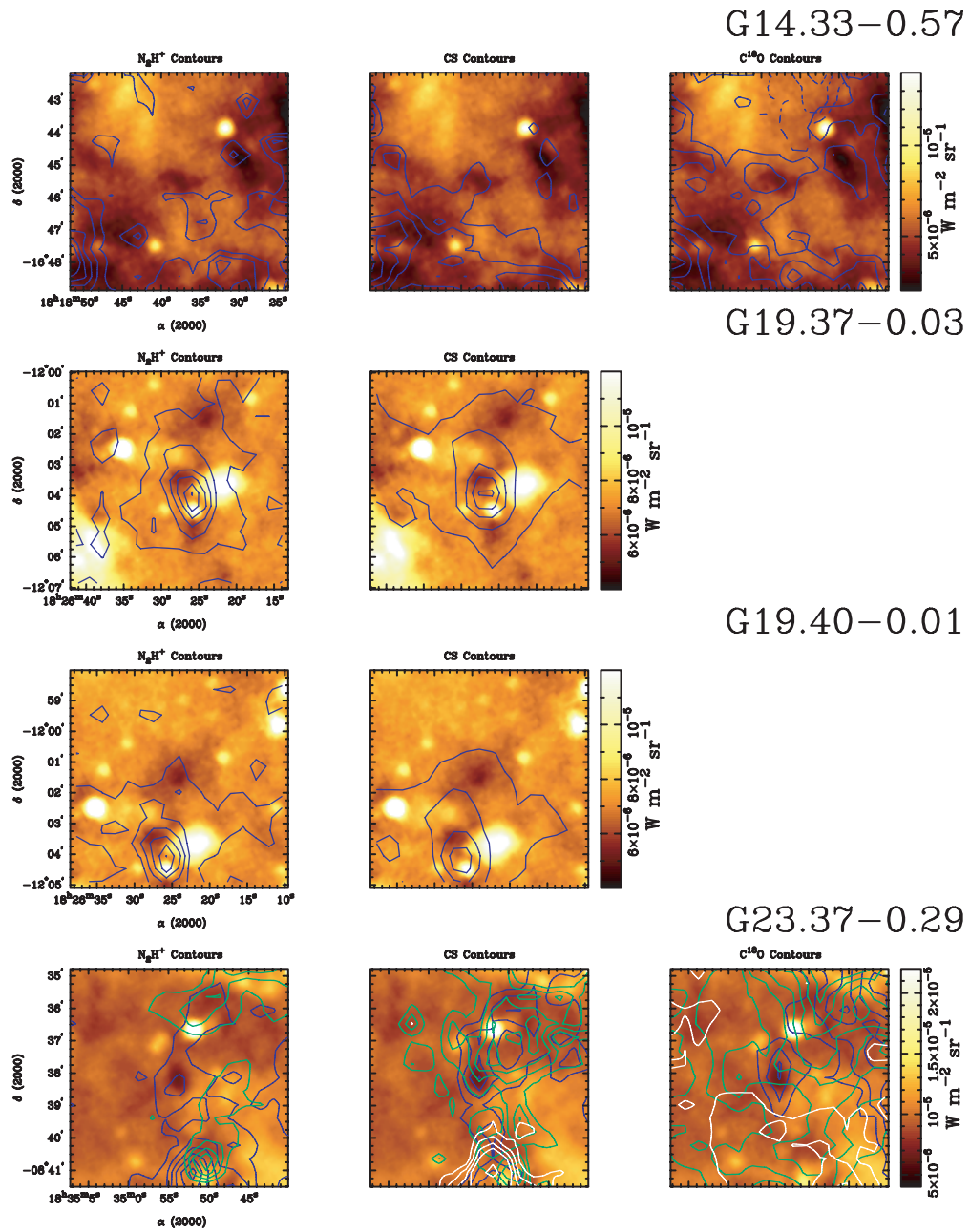


FIG. 1.—Continued

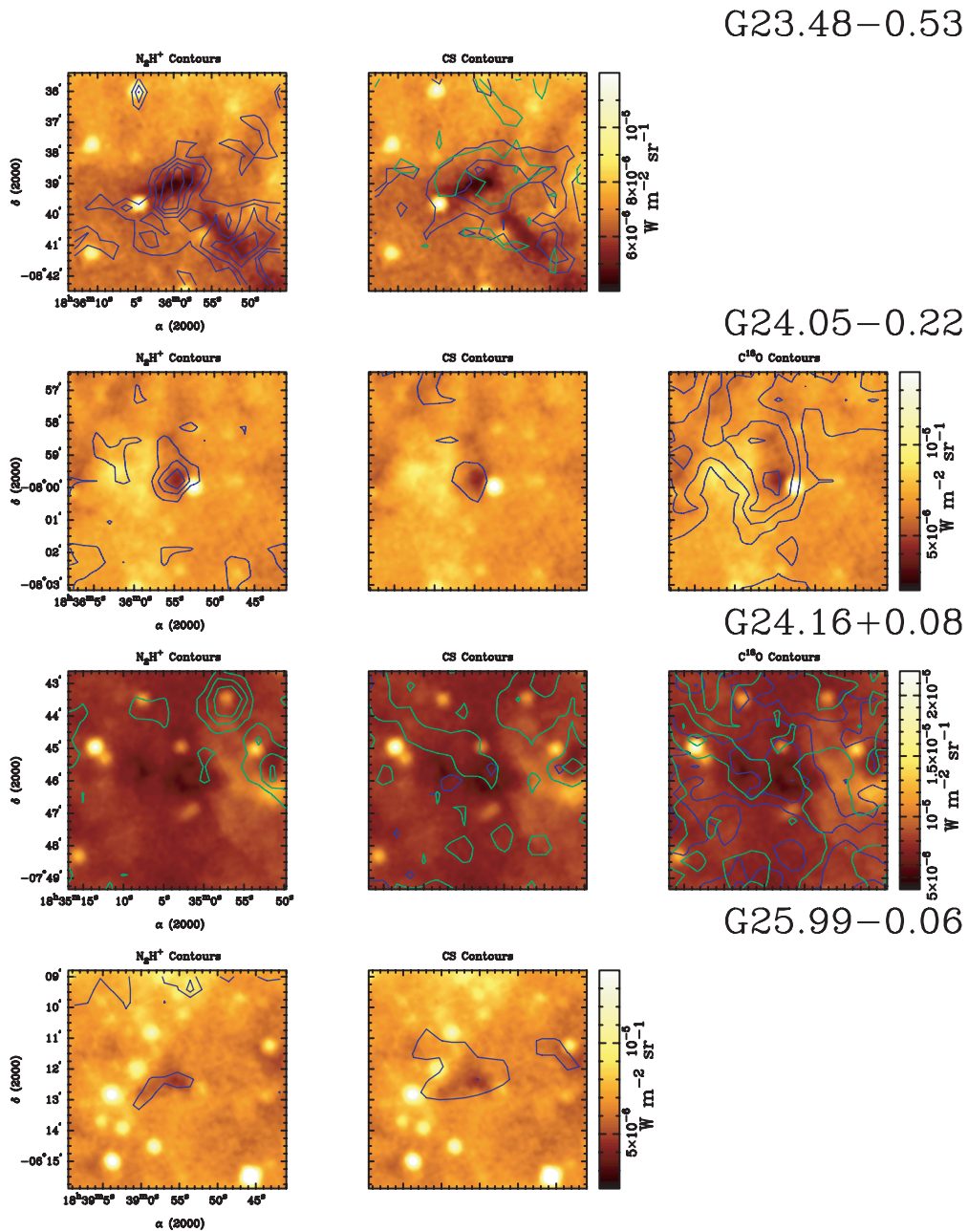
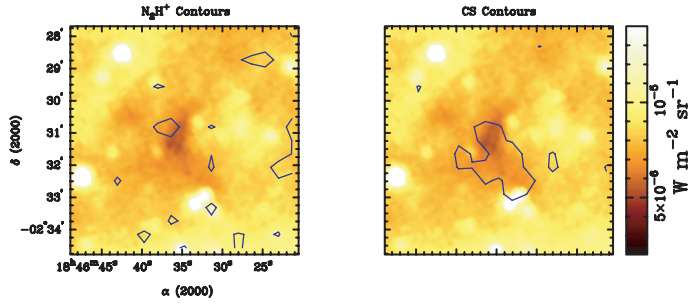
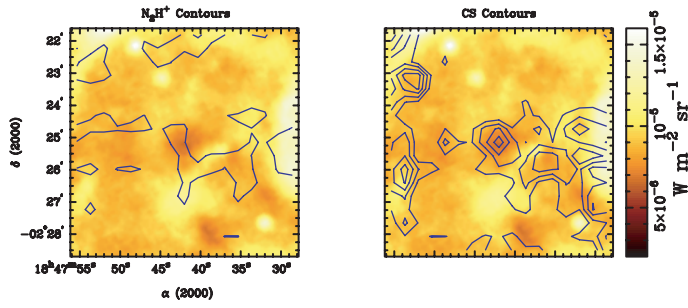


FIG. 1.— *Continued*

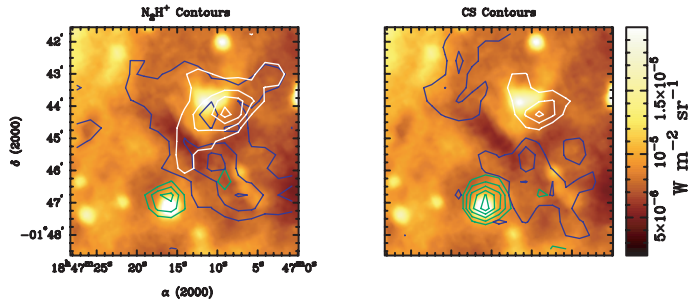
G30.14-0.07



G30.53-0.27



G30.89+0.14



G30.98-0.15

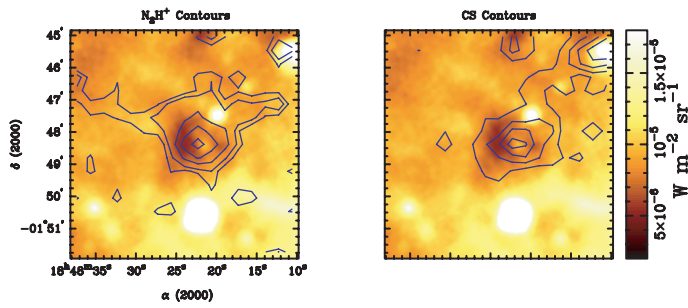


FIG. 1.—*Continued*

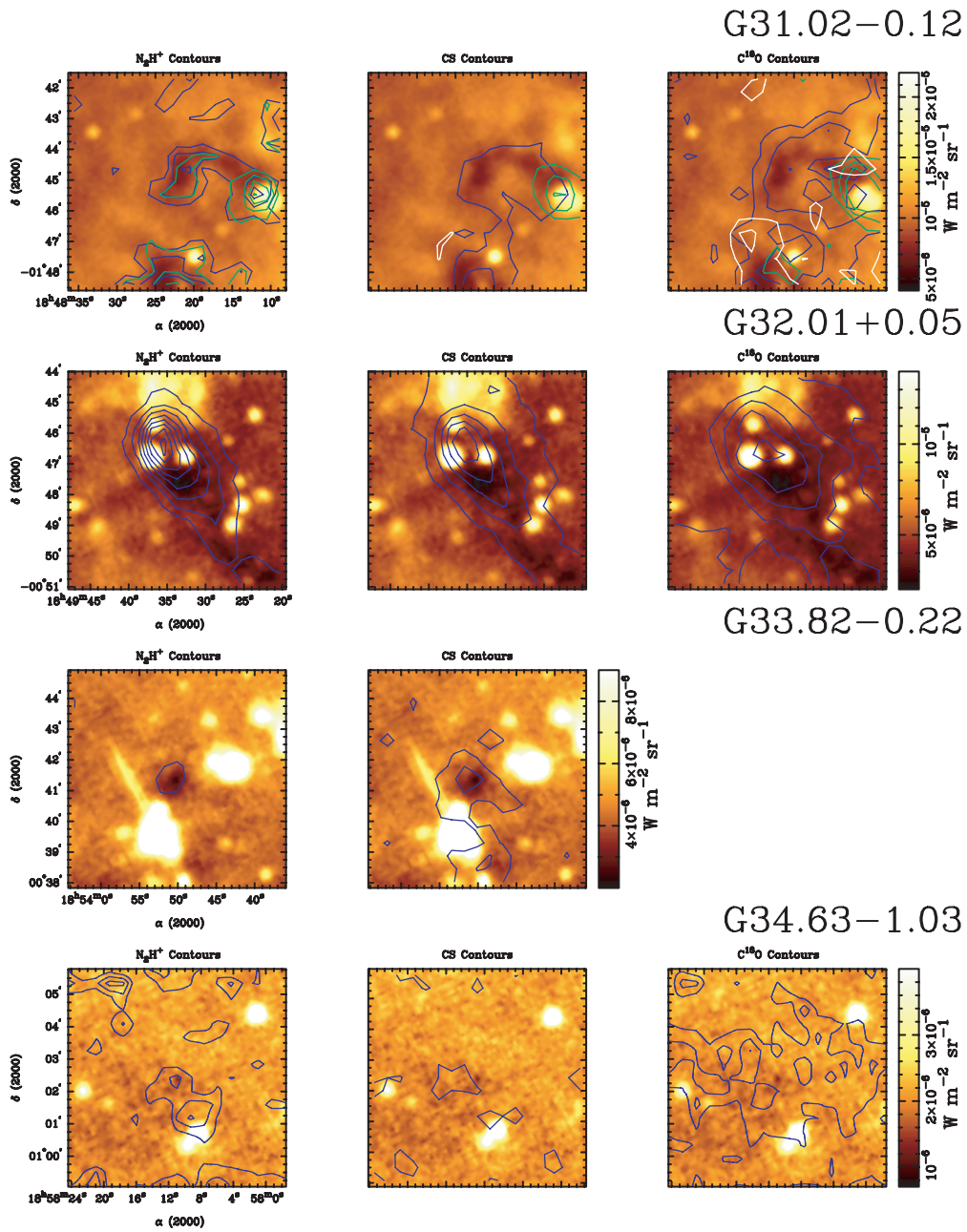


FIG. 1.— *Continued*

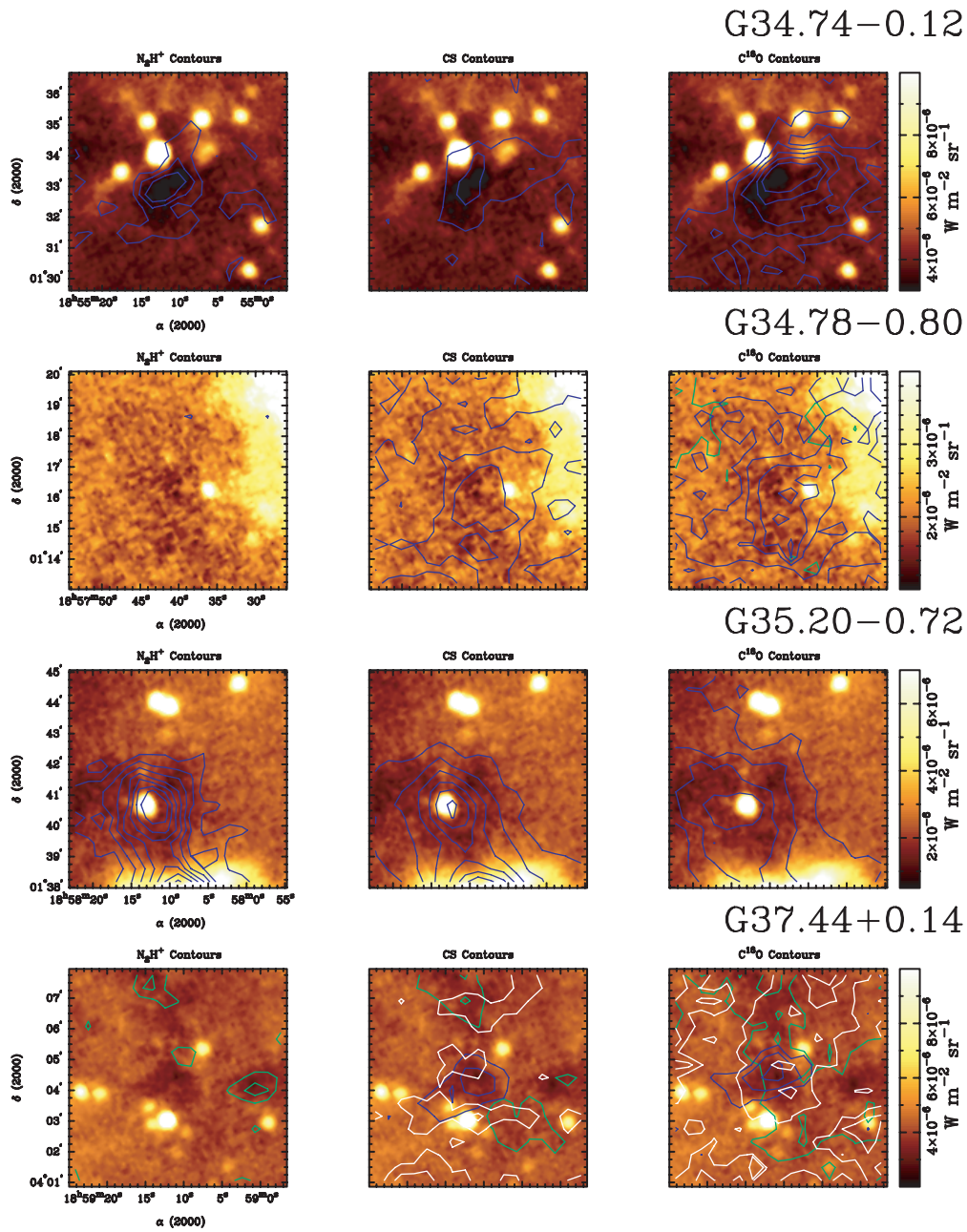


FIG. 1.—*Continued*

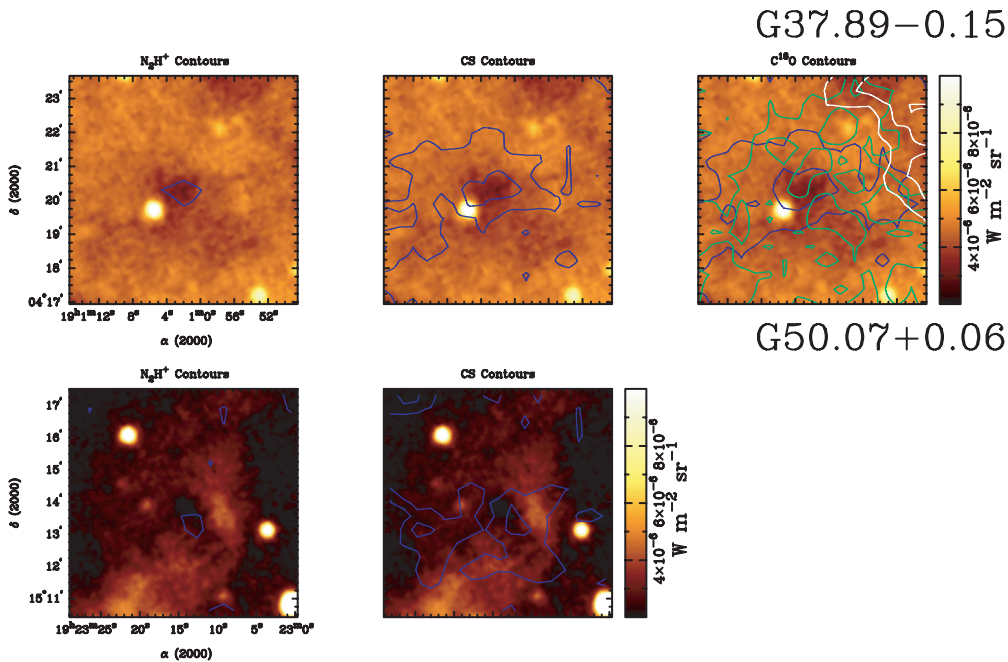


FIG. 1.—Continued

to the UC H II region (12.0 kpc). In this case, it is likely that we are detecting two clouds along the same line of sight at different distances: one near the UC H II region and one nearer to us. Since the emission of the primary component corresponds so well to the absorbing dark cloud, we maintain that these lie at the “near” distances, although there is significant uncertainty in the distance calculation. Nonetheless, as we will show, these clouds are massive and are likely associated with the formation of intermediate- and high-mass stars and stellar clusters.

3.4. Column Densities and Densities

To determine the molecular abundances relative to molecular hydrogen, we also need a measure of the total H_2 column density. We estimate $N(H_2)$ from the *MSX* images convolved to match the FCRAO beam resolution and the simple relation $\tau_\lambda = \sigma_\lambda \cdot N(H_2)$, where τ_λ is the dust opacity, σ_λ is the dust extinction cross section, and $N(H_2)$ is the column density of molecular hydrogen. The behavior of the mid-infrared extinction law is an area of active research. Recent results from Indebetouw et al. (2005) show agreement with Weingartner & Draine (2001) ($R_v = 5.5$, “case B”), and we therefore adopt a value for σ_λ at $8.8 \mu\text{m}$ of $2.3 \times 10^{-23} \text{ cm}^2$, although this value can be considered reliable only within a factor of 2. The opacity, τ_λ , is roughly estimated by examining the relative intensities of the average background ($I_{o,\lambda}$) and central core (I_λ), assuming that $I_\lambda = I_{o,\lambda} e^{-\tau_\lambda}$ (i.e., no emission by the core itself). The ratio $I_\lambda/I_{o,\lambda}$ is related, but not identical, to the brightness contrast listed in Table 1, since the values listed in Table 1 do not incorporate the convolution to the FCRAO beam, and are provided at the original *MSX* resolution.

The column densities of $C^{18}O$ and CS are estimated by assuming that the cores are in local thermodynamic equilibrium (LTE) at a temperature of 15 K and that the emission is optically thin (Table 4). While the optically thin assumption is probably reasonable for $C^{18}O$, it probably does not hold for CS, which generally has optically thick emission in the interstellar medium. For N_2H^+ , the fits to the hyperfine components generally suggest low optical depth, or $\tau \sim 1$. However, its emission is likely not in

LTE. At a density of 10^5 cm^{-3} , the fractional population will be underestimated by a factor of ~ 1.7 relative to LTE; we therefore apply this correction factor. We also crudely estimate the gas density by assuming the cloud is spherical and dividing the H_2 column density by the diameter of the cloud (using the sizes listed in Table 1 and the distances in Table 3). This gives an average density of $\approx 5000 \text{ cm}^{-3}$. This is well below the average densities found in other studies of regions of massive star formation using other tracers. For example, Plume et al. (1997) surveyed multiple transitions of CS in 150 H_2O masers (used as signposts of massive star formation) and found an average gas density of $7.9 \times 10^5 \text{ cm}^{-3}$. An obvious explanation for the lower density in our sample is that the clouds are not spherical, as we have naively assumed, and may instead be clumpy on scales below our resolution. Moreover, these objects are likely at an earlier evolutionary state, which is characterized by lower densities. A more detailed analysis of the density and column density will be presented in future work (D. L. Gibson et al. 2007, in preparation).

3.5. Masses

The total mass of each dark cloud is estimated using an assumed (“near”) distance, an approximate size based on the extent of molecular emission, the molecular column densities, and approximate abundance calculated at the peak of absorption. Table 4 lists the masses of the objects for which there is a significant detection of N_2H^+ or $C^{18}O$ (or both) and a distance could be assigned. Since some of the dark clouds shown in Figure 1 have a different structure when viewed in different molecular tracers and may have different opacities, we have, for completeness, estimated the masses independently based on the abundances derived from both the N_2H^+ and $C^{18}O$ data. Our average mass is $\approx 2000\text{--}3000 M_\odot$ (depending on whether the N_2H^+ or $C^{18}O$ mass is used).

Figure 2 shows how the masses of our sample compare to the high-mass protostellar objects (HMPOs) presented in Williams et al. (2004), which were determined from submillimeter continuum emission. The masses for the HMPO sample are shown

TABLE 3
KINEMATIC DISTANCES TO SEPARATED VELOCITY COMPONENTS

Source	Velocity Component (km s ⁻¹)	Near Distance (kpc)	Far Distance (kpc)	Adopted Distance (kpc)	UC H II Region Distance (kpc)
G05.85−0.23.....	17	3.14 ^{+0.66} _{−0.76}	13.78 ^{+0.75} _{−0.67}	3.14	2.6
	9	1.53 ^{+0.86} _{−0.96}	15.38 ^{+0.97} _{−0.86}		
G06.26−0.51.....	23	3.78 ^{+0.59} _{−0.67}	13.12 ^{+0.67} _{−0.60}	3.78	2.6
	17	3.01 ^{+0.68} _{−0.77}	13.89 ^{+0.77} _{−0.68}		
G09.16+0.06.....	31	3.81 ^{+0.61} _{−0.69}	12.97 ^{+0.69} _{−0.61}	3.81	6.2
G09.21−0.22.....	43	4.57 ^{+0.53} _{−0.59}	12.21 ^{+0.59} _{−0.53}	4.57	6.2
G09.28−0.15.....	42	4.48 ^{+0.54} _{−0.61}	12.30 ^{+0.61} _{−0.54}	4.48	6.2
G09.86−0.04.....	18	2.36 ^{+0.78} _{−0.88}	14.39 ^{+0.87} _{−0.78}	2.36	6.0
G10.99−0.09.....	30	3.31 ^{+0.69} _{−0.76}	13.37 ^{+0.77} _{−0.68}	3.31	6.0
G12.22+0.14.....	40	3.75 ^{+0.65} _{−0.72}	12.86 ^{+0.73} _{−0.65}	3.75	5.2
G12.50−0.22.....	36	3.55 ^{+0.67} _{−0.75}	13.05 ^{+0.75} _{−0.67}	3.55	5.2
G14.33−0.57.....	19	1.99 ^{+0.85} _{−0.95}	14.48 ^{+0.95} _{−0.85}	1.99	2.1
	20	2.04 ^{+0.85} _{−0.94}	14.43 ^{+0.94} _{−0.85}	2.04	
G19.37−0.03.....	27	2.26 ^{+0.88} _{−0.98}	13.78 ^{+0.97} _{−0.88}	2.26	4.5
G19.40−0.01.....	27	2.23 ^{+0.88} _{−0.98}	13.81 ^{+0.97} _{−0.89}	2.23	4.5
G23.37−0.29.....	78	4.70 ^{+0.90} _{−0.88}	10.91 ^{+0.88} _{−0.91}	4.70	9.0
	103	5.69 ^{+1.20} _{−0.91}	9.91 ^{+0.92} _{−1.20}		
G23.48−0.53.....	65	4.13 ^{+0.88} _{−0.89}	11.47 ^{+0.90} _{−0.87}		
	64	4.10 ^{+0.88} _{−0.90}	11.50 ^{+0.89} _{−0.89}	4.10	9.0
G24.05−0.22.....	76	4.60 ^{+0.91} _{−0.88}	10.99 ^{+0.88} _{−0.91}		
	82	4.82 ^{+0.96} _{−0.90}	10.70 ^{+0.91} _{−0.96}	4.82	9.0
G24.16+0.08.....	53	3.46 ^{+0.91} _{−0.94}	12.05 ^{+0.94} _{−0.91}	3.46	9.0
	113	6.13 _{−1.03}	9.38		
G25.99−0.06.....	90	5.15 ^{+1.23} _{−0.99}	10.13 ^{+0.99} _{−1.23}	5.15	14.0
G30.89+0.14.....	96	5.65 _{−1.38}	8.93	5.65	8.5
	40	2.62 ^{+1.14} _{−1.15}	11.97 ^{+1.15} _{−1.14}		
G30.98−0.15.....	108	6.65 _{−1.84}	7.94		
	78	4.63 ^{+1.63} _{−1.19}	9.94 ^{+1.19} _{−1.62}	4.63	8.5
G31.02−0.12.....	76	4.56 ^{+1.56} _{−1.19}	10.01 ^{+1.19} _{−1.56}	4.56	8.5
	83	4.90 _{−1.23}	9.67		
G32.01+0.05.....	92	5.41 _{−1.33}	9.16		
	95	5.77 _{−1.51}	8.64	5.77	8.5
G34.63−1.03.....	14	0.84 ^{+1.26}	13.14 ^{+1.32} _{−1.26}	3.2	
G34.74−0.12.....	79	4.86 _{−1.45}	9.11	4.86	3.7
G34.78−0.80.....	44	2.80 ^{+1.33} _{−1.26}	11.17 ^{+1.25} _{−1.33}	2.80	3.2
	37	2.41 ^{+1.28} _{−1.26}	11.56 ^{+1.26} _{−1.29}		
G35.20−0.72.....	33	2.17 ^{+1.29} _{−1.28}	11.73 ^{+1.27} _{−1.30}	2.17	3.2
	40	2.59 ^{+1.47} _{−1.34}	10.91 ^{+1.34} _{−1.47}	2.59	12.0
G37.44+0.14.....	18	1.16 ^{+1.34}	12.34 ^{+1.36} _{−1.34}		
	86	5.90 _{−2.12}	7.60		
G37.89−0.15.....	13	0.82 ^{+1.35}	12.60 ^{+1.38} _{−1.35}	0.82	12.0
	65	4.16 _{−1.51}	9.26		
	86	6.09 _{−2.31}	7.33		

for both their “near” and “far” kinematic distances. Assuming that the sample encompasses objects at both the “near” and “far” kinematic distances, then the derived masses for HMPOs show a comparable range to our sources.

One caveat with our comparison to the Williams et al. sample lies in the selection bias of our sample. As we will discuss below, our observations are only sensitive to relatively massive objects when the cores reside at such large distances. Furthermore, the HMPOs in the Williams et al. study also contain protostars that heat the surrounding environment and increase the dust emission. Therefore, in the warmer environments of the Williams et al. survey, lower mass cores would be easier to detect. The mass distribution shown in Figure 2 also shows good agreement with that found by Shirley et al. (2003), who observed CS emission from a sample of massive star-forming regions and found a mean mass of 920 M_{\odot} with a large dispersion.

Several assumptions contribute to the uncertainty in the mass calculation, which is dominated by the error in the abundance calculation. We assume a constant temperature of 15 K, and a 5 K change in this value results in a $\sim 20\%$ change in the abundance. The uncertainty in the dust opacity/column density relation contributes another factor of 2. Finally, we assume a constant abundance along the line of sight, which likely contributes an additional factor of 2–3 to the mass estimates.

We note that the typical distance to these clouds is ~ 4 kpc, and with $50''$ resolution, we are likely only sensitive to objects of some minimum mass. To examine this limit, we modeled the emission of a cloud assuming a constant density of 10^5 cm⁻³, a radius of 0.1 pc, and an N₂H⁺ abundance of 5×10^{-10} using a Monte Carlo radiation transfer model (Ashby et al. 2000). We estimate that our observations are capable of detecting clouds of mass greater than 50–100 M_{\odot} at a distance of 4 kpc with a $50''$ beam.

TABLE 4
MOLECULAR ABUNDANCES AND CLOUD MASSES

SOURCE	DISTANCE ^a (kpc)	$N(\text{H}_2)$ (10^{21}cm^{-2})	ABUNDANCE RELATIVE TO H_2			CLOUD MASS	
			N_2H^+	C^{18}O	CS	(M_\odot) ^b	(M_\odot) ^c
G05.85–0.23.....	3.14	4.4 ± 0.9	$2.9\text{E}-10$	$3.5\text{E}-7$	$5.0\text{E}-10$	$2.6\text{E}+2$	$2.5\text{E}+2$
G06.26–0.51.....	3.78	13.5 ± 1.2	...	$1.3\text{E}-7$	$5.6\text{E}-10$...	$6.2\text{E}+3$
G09.16+0.06.....	3.81	4.4 ± 1.6	...	$3.4\text{E}-7$	$4.2\text{E}-10$...	$3.3\text{E}+3$
G09.21–0.22.....	4.57	1.9 ± 1.2	$2.0\text{E}-9$...	$3.2\text{E}-9$	$1.4\text{E}+3$...
G09.28–0.15.....	4.48	7.5 ± 1.2	$5.2\text{E}-10$...	$7.9\text{E}-10$	$3.4\text{E}+3$...
G09.86–0.04.....	2.36	9.8 ± 1.0	$9.4\text{E}-11$...	$7.2\text{E}-10$	$1.5\text{E}+3$...
G10.99–0.09.....	3.32	8.1 ± 0.9	$5.5\text{E}-10$	$3.0\text{E}-7$	$5.7\text{E}-10$	$2.0\text{E}+3$	$4.3\text{E}+3$
G12.22+0.14.....	3.75	2.8 ± 1.0	$1.4\text{E}-9$...	$3.0\text{E}-9$	$3.2\text{E}+2$...
G12.50–0.22.....	3.55	4.8 ± 1.7	$6.5\text{E}-10$	$3.6\text{E}-7$	$1.4\text{E}-9$	$5.4\text{E}+2$	$7.1\text{E}+3$
G14.33–0.57a.....	1.99	4.1 ± 0.4	...	$5.7\text{E}-7$	$1.4\text{E}-9$...	$8.3\text{E}+2$
G14.33–0.57b.....	2.05	3.4 ± 1.1	$4.4\text{E}-10$	$5.7\text{E}-7$	$1.1\text{E}-9$	$1.3\text{E}+3$	$1.2\text{E}+3$
G19.37–0.03.....	2.26	2.2 ± 1.5	$1.7\text{E}-9$...	$6.4\text{E}-9$	$2.8\text{E}+2$...
G19.40–0.01.....	2.23	4.9 ± 1.0	$2.1\text{E}-10$...	$7.7\text{E}-10$	$2.1\text{E}+3$...
G23.37–0.20.....	4.70	3.4 ± 1.1	$9.0\text{E}-10$	$1.2\text{E}-6$	$3.1\text{E}-9$	$3.3\text{E}+3$	$4.1\text{E}+3$
G23.48–0.53a.....	4.10	7.8 ± 3.3	$2.0\text{E}-10$...	$5.4\text{E}-10$	$2.7\text{E}+3$...
G23.48–0.53b.....	4.02	5.7 ± 1.4	$2.3\text{E}-10$...	$6.0\text{E}-10$	$2.0\text{E}+3$...
G24.05–0.22.....	4.82	2.7 ± 1.4	$1.1\text{E}-9$	$9.1\text{E}-7$	$1.7\text{E}-9$	$4.0\text{E}+2$	$2.1\text{E}+3$
G24.16+0.08.....	3.46	4.0 ± 1.4	...	$4.4\text{E}-7$	$2.6\text{E}+3$
G25.99–0.06.....	5.15	4.1 ± 1.5	$2.1\text{E}-10$...	$1.2\text{E}-9$	$6.8\text{E}+2$...
G30.89+0.14.....	5.65	4.2 ± 1.0	$3.2\text{E}-10$...	$6.2\text{E}-10$	$1.1\text{E}+4$...
G30.98–0.15.....	4.63	7.3 ± 2.7	$6.6\text{E}-10$...	$1.4\text{E}-9$	$1.9\text{E}+3$...
G31.02–0.12.....	4.56	4.3 ± 0.9	$3.9\text{E}-10$	$3.1\text{E}-7$	$7.1\text{E}-10$	$2.6\text{E}+3$	$4.7\text{E}+3$
G32.01+0.05.....	5.77	7.3 ± 2.3	$1.0\text{E}-9$	$6.5\text{E}-7$	$2.6\text{E}-9$	$8.7\text{E}+3$	$1.3\text{E}+4$
G34.63–1.03.....	0.84	3.6 ± 1.0	$3.4\text{E}-10$	$1.7\text{E}-7$...	$5.5\text{E}+1$	$6.0\text{E}+1$
G34.74–0.12.....	4.86	5.1 ± 1.5	$4.0\text{E}-10$	$7.3\text{E}-7$	$1.0\text{E}-9$	$8.7\text{E}+2$	$2.4\text{E}+3$
G34.78–0.80.....	2.80	6.1 ± 3.8	$5.7\text{E}-11$	$3.9\text{E}-7$	$1.4\text{E}-9$...	$2.9\text{E}+3$
G35.20–0.72.....	2.17	3.5 ± 2.5	$9.2\text{E}-10$	$6.2\text{E}-7$	$2.5\text{E}-9$	$1.0\text{E}+3$	$1.5\text{E}+3$
G37.44+0.14a.....	2.59	3.0 ± 1.5	...	$4.0\text{E}-7$	$1.2\text{E}-9$...	$8.9\text{E}+1$
G37.44+0.14b.....	1.16	2.6 ± 0.9	$2.6\text{E}-10$	$2.1\text{E}-7$	$4.5\text{E}-10$	$3.2\text{E}+1$	$1.1\text{E}+2$
G37.89–0.15.....	0.82	3.2 ± 1.6	$1.5\text{E}-10$	$2.1\text{E}-7$	$5.2\text{E}-10$	$3.7\text{E}+0$	$5.4\text{E}+1$

^a Distances from rotation curve of Fich et al. (1989), assuming absorbing cloud lies at near distance.

^b From N_2H^+ .

^c From C^{18}O .

Assuming that the “near” distance assumption is correct, the uncertainties mentioned above can account for up to a factor of $\sim 4\text{--}6$ in mass error, as the 14% error in translating the Galactic rotation curve to kinematic distances only introduces a distance error of $\sim 20\%$. This accounting suggests that these objects are

at least $100 M_\odot$, and likely an order of magnitude more massive. Should the “near” distance assumption be incorrect and the dark clouds lie closer to the “far” kinematic distance, then the distance error dominates the calculation, and these clouds are substantially more massive.

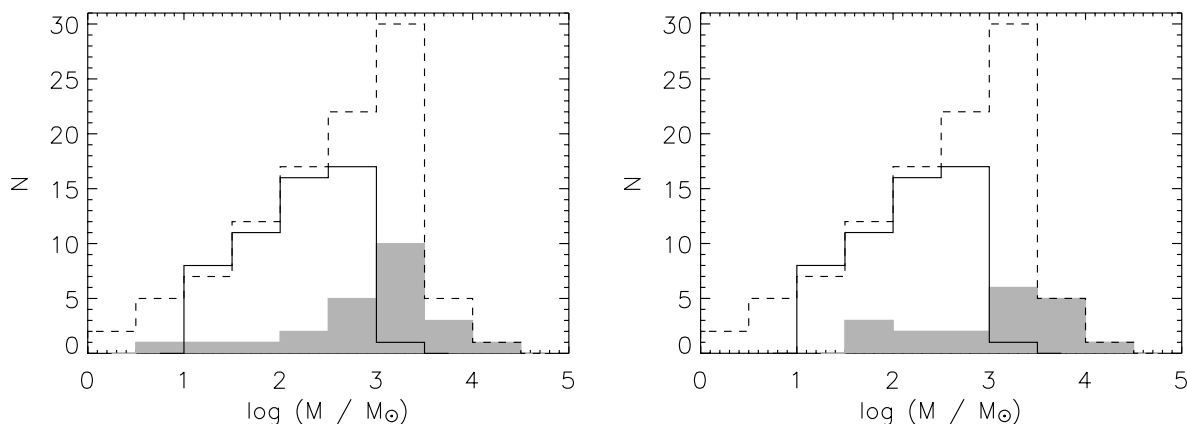


FIG. 2.—Histogram of the mass distribution for our sample of IR dark cores as derived from the N_2H^+ data (left panel) and the C^{18}O data (right panel). The gray histograms show the mass distribution for our sample of cores, whereas the solid line shows the distribution of masses of the Williams et al. (2004) cores (derived from $850 \mu\text{m}$ data) based on the near Galactic distances. The dashed line represents the masses based on the far Galactic distances.

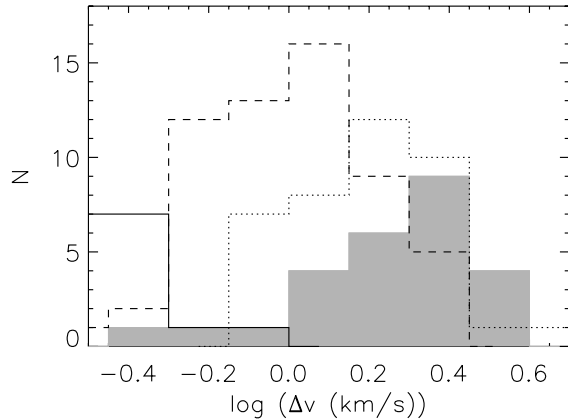


FIG. 3.—Histogram of the N_2H^+ (solid line, Caselli et al. 2002; gray, this sample) and NH_3 (dashed line; Harju et al. 1993; dotted line; Molinari et al. 1996) line widths.

3.6. Velocity Dispersion

The width of emission lines in star-forming clouds serves as a useful diagnostic in determining the nature of a molecular region. According to Goldsmith (1987), the sites of massive star formation, GMCs, are characterized by large line widths, while the isolated sites of low-mass star formation, dark clouds, have considerably smaller line widths. We illustrate this range in Figure 3.

Caselli et al. (2002) derived line widths for N_2H^+ for a sample of low-mass, dense clumps in dark clouds, a site in which we expect to find narrow lines. The average line width in the Caselli et al. study was 0.33 km s^{-1} for clumps in which no *IRAS* source is detected. Current chemical models and observations indicate that NH_3 and N_2H^+ are related because NH_3 likely forms via pathways linked N_2H^+ (Aikawa et al. 2005). Therefore, we use the Harju et al. (1993) line widths for NH_3 clumps in Orion and Cepheus, known to be large regions of clustered, high-mass star formation for comparison. In addition, we include a comparison with line widths of a sample of ammonia cores presented in Molinari et al. (1996), although we only include only the “Low” sources, a sample they argue has less luminous *IRAS* sources and more quiescent envelopes and, therefore, are younger than their “High” counterparts. In our sample, we find average line widths of 2.0 km s^{-1} for N_2H^+ , 2.1 km s^{-1} for C^{18}O , and 2.9 km s^{-1} for CS. Although we see a broad range of line widths in the N_2H^+ observations of the dark clouds, the characteristic line widths presented here are generally higher than those of the Harju et al. study and, to a greater extent, the Caselli et al. study, which implies that the objects in this sample are likely not associated

with low-mass star formation. However, we find good agreement with the Molinari et al. sample.

For the CS $J = 2 \rightarrow 1$ transition, the line widths in the dark cloud sample are narrower than those observed by Plume et al. (1997) in survey of massive star-forming regions, which averaged 4.2 km s^{-1} in this line. However, since Plume et al. surveyed regions known to have undergone massive star formation, it is possible that the current generation of massive stars are injecting additional turbulence into the surrounding environment. Similarly, the Shirley et al. (2003) study observed the CS $J = 5 \rightarrow 4$ transition in star-forming cores and found line widths averaging 5.6 km s^{-1} . The narrower lines in the dark clouds indicates that they are still relatively quiescent and suggest that they may, indeed, be precursor sites of intermediate or massive star formation.

4. SUMMARY

We have identified 41 infrared dark (at $8.8 \mu\text{m}$) clouds that are opaque, compact, and associated with UC H II regions using *MSX* survey data. In order to determine some basic characteristics of these dark clouds, we have mapped emission from N_2H^+ $1 \rightarrow 0$, CS $2 \rightarrow 1$, and C^{18}O $1 \rightarrow 0$ using the FCRAO. The morphology and relative strengths of these molecular lines varies dramatically, possibly indicating evolutionary differences and/or the presence of undetected embedded protostar(s). Based on the derived kinematic distances and the simplifying assumption that the cores are optically thin, we have determined average properties: diameter $\langle D \rangle \approx 0.9 \text{ pc}$, density $\langle n \rangle \approx 5000 \text{ cm}^{-3}$, and mass $\langle M \rangle \approx 2500 M_\odot$. The low-density estimate likely indicates that the dark clouds are clumpy rather than homogeneous. The derived masses, however, are comparable to those derived for a sample of HMPOs. The line widths are larger than those seen in low-mass star-forming cores and larger than in high-mass star-forming cores in Orion and Cepheus. However, they are narrower than the CS line widths seen in regions that are actively forming massive stars. These observations, taken together, suggest that the infrared dark clouds may be the relatively quiescent precursors to intermediate or massive star formation, the so-called “pre-protostellar cores.” At present, we do not know if these sources are truly starless. Only by obtaining very sensitive infrared observations can we confirm the starless nature of these cores.

We are grateful to the referee for a very thorough report, which improved this paper. We are grateful to J. Weingartner for providing detailed dust opacity coefficients. This research has made use of the SIMBAD database, operated at CDS, Strasbourg, France.

APPENDIX

COINCIDENT SOURCES

The coordinates of each dark region were examined by the Set of Identifications, Measurements, and Bibliography for Astronomical Data (SIMBAD) database in search of associated objects indicative of active star formation (e.g., masers, *IRAS* sources, radio sources). In most cases, the searches yielded no results, but some revealed objects within one arcminute of the dark region’s coordinates. Below, we summarize any associations with the objects for which we present emission maps. We note that whenever coincident sources are found, we provide the offsets relative to the central absorption peak position given in Table 1.

G09.21–0.22.—There is an *IRAS* source [IRAS 18038–2105; $\alpha(\text{J2000.0}) = 18^{\text{h}}06^{\text{m}}53^{\text{s}}.1$, $\delta(\text{J2000.0}) = -21^{\circ}04'38''$] in the vicinity of this absorbing cloud, offset by 0.78 from the center of the dark region.

G09.88–0.11.—This region has an associated 1612 MHz OH maser that is cited in Blommaert et al. (1994). This source, OH 9.878–0.127, has a position of $\alpha(\text{J2000.0}) = 18^{\text{h}}07^{\text{m}}59^{\text{s}}.07$, $\delta(\text{J2000.0}) = -20^{\circ}27'34''.3$, which is offset from the center of our region by $1'.05$. This object may be associated with a circumstellar shell around an evolved star, and the velocities believed to correspond to the

expanding shells of material are 79.5 and 111.3 km s⁻¹, which is not coincident with the velocity of the emission detected here (17 km s⁻¹).

G10.59–0.31.—This region contains a radio source, located at $\alpha(\text{J2000.0}) = 18^{\text{h}}10^{\text{m}}6^{\text{s}}18$, $\delta(\text{J2000.0}) = -19^{\circ}55'33''11$, according to Zoonematkermani et al. (1990), which is offset from the center of our region by 0'.44.

G12.50–0.22.—There is an *IRAS* source [*IRAS* 18197–1812; $\alpha(\text{J2000.0}) = 18^{\text{h}}13^{\text{m}}39^{\text{s}}0$, $\delta(\text{J2000.0}) = -18^{\circ}11'46''$] offset by 0'.96 from the absorbing region.

G19.37–0.03.—This region is near a known UC H II region, with a water and methanol maser (Codella & Felli 1995; Szymczak et al. 2000) also identified in the vicinity [$\alpha(\text{J2000.0}) = 18^{\text{h}}26^{\text{m}}24^{\text{s}}3$, $\delta(\text{J2000.0}) = -12^{\circ}3'46''$] offset 0'.85 from the absorbing region. The peak velocity of this maser is 26.3 km s⁻¹ (Szymczak et al. 2000), which is consistent with the velocity of our measured emission (27 km s⁻¹). Molinari et al. (1996) also observed this maser site and designated it as Mol 55.

G30.89+0.14.—This region has an associated methanol maser, as described by Szymczak et al. (2000). The maser is located at $\alpha(\text{J2000.0}) = 18^{\text{h}}47^{\text{m}}14^{\text{s}}99$, $\delta(\text{J2000.0}) = -1^{\circ}44'7''99$, which is offset from the center of our region by 0'.99. Szymczak et al. (2000), using a 6.7 GHz survey, measured the internal velocity of the maser source to be ≈ 105 km s⁻¹, the velocity of the peak to be 101.5 km s⁻¹. This is consistent with one of the velocity components we measured in this object (108 km s⁻¹).

G32.01+0.05.—This region has an associated *IRAS* point source (18470–0050) that is offset from the center of our region by 1'.00 at $\alpha(\text{J2000.0}) = 18^{\text{h}}49^{\text{m}}36^{\text{s}}6$, $\delta(\text{J2000.0}) = -00^{\circ}46'51''$, which coincides with a radio source (Becker et al. 1994). This was confirmed to be a methanol maser (observed in the velocity range between 91 and 102 km s⁻¹) by van der Walt et al. (1995), which is consistent with the emission we observed at 95 km s⁻¹.

G34.74–0.12.—This region has an associated *IRAS* point source (18526+0130) that is offset from the center of our region by 0'.80 at $\alpha(\text{J2000.0}) = 18^{\text{h}}55^{\text{m}}10^{\text{s}}$, $\delta(\text{J2000.0}) = +1^{\circ}33'57''$.

REFERENCES

- Aikawa, Y., Herbst, E., Roberts, H., & Caselli, P. 2005, *ApJ*, 620, 330
 Alves, J. F., Lada, C. J., & Lada, E. A. 2001, *Nature*, 409, 159
 André, P., Ward-Thompson, D., & Barsony, M. 2000, *Protostars and Planets IV*, ed. V. Mannings, A. P. Boss, & S. S. Russell (Tucson: Univ. Arizona Press), 59
 Ashby, M. L. N., et al. 2000, *ApJ*, 539, L115
 Bacmann, A., André, P., Puget, J.-L., Abergel, A., Bontemps, S., & Ward-Thompson, D. 2000, *A&A*, 361, 555
 Becker, R. H., White, R. L., Helfand, D. J., & Zoonematkermani, S. 1994, *ApJS*, 91, 347
 Beichman, C. A., Myers, P. C., Emerson, J. P., Harris, S., Mathieu, R., Benson, P. J., & Jennings, R. E. 1986, *ApJ*, 307, 337
 Bergin, E. A., & Langer, W. D. 1997, *ApJ*, 486, 316
 Blommaert, J. A. D. L., van Langevelde, H. J., & Michiels, W. F. P. 1994, *A&A*, 287, 479
 Buisson, G., Desbats, L., Duvert, G., Forveille, T., Gras, R., Guilloteau, S., Lucas, R., & Valiron, P. 2002, *Continuum and Line Analysis Single-Dish System Manual (CLASS; Grenoble: IRAM)* (<http://iram.fr/GS/class/class.html>)
 Carey, S. J., Clark, F. O., Egan, M. P., Price, S. D., Shipman, R. F., & Kuchar, T. A. 1998, *ApJ*, 508, 721
 Caselli, P., Benson, P., Myers, P., & Tafalla, M. 2002, *ApJ*, 572, 238
 Codella, C., & Felli, M. 1995, *A&A*, 302, 521
 Egan, M. P., Shipman, R. F., Price, S. D., Carey, S. J., Clark, F. O., & Cohen, M. 1998, *ApJ*, 494, L199
 Fich, M., Blitz, L., & Stark, A. 1989, *ApJ*, 342, 272
 Garay, G., & Lizano, S. 1999, *PASP*, 111, 1049
 Goldsmith, P. 1987, in *Interstellar Processes* (Dordrecht: Reidel), 51
 Harju, J., Walmsley, C. M., & Wouterloot, J. G. A. 1993, *A&AS*, 98, 51
 Indebetouw, R., et al. 2005, *ApJ*, 619, 931
 Jørgensen, J. K. 2004, *A&A*, 424, 589
 Lee, C. W., & Myers, P. C. 1999, *ApJS*, 123, 233
 Lee, J.-E., Bergin, E. A., & Evans, N. J. 2004, *ApJ*, 617, 360
 Menten, K. M., Pillai, T., & Wyrowski, F. 2005, *IAU Symp.* 227, *Massive Star Birth: A Crossroads of Astrophysics*, ed. R. Cesaroni et al. (Cambridge: Cambridge Univ. Press), 23
 Molinari, S., Brand, J., Cesaroni, R., & Palla, F. 1996, *A&A*, 308, 573
 Myers, P. C., & Benson, P. J. 1983, *ApJ*, 266, 309
 Pillai, T., Wyrowski, F., Carey, S. J., & Menten, K. M. 2006, *A&A*, 450, 569
 Plume, R., Jaffe, D. T., Evans, N. J., II, Martín-Pintado, J., & Gómez-González, J. 1997, *ApJ*, 476, 730
 Rathborne, J. M., Jackson, J. M., & Simon, R. 2006, *ApJ*, 641, 389
 Shirley, Y. L., Evans, N. J., II, Young, K. E., Knez, C., & Jaffe, D. T. 2003, *ApJS*, 149, 375
 Sridharan, T. K., Beuther, H., Saito, M., Wyrowski, F., & Schilke, P. 2005, *ApJ*, 634, L57
 Szymczak, M., Hrynek, G., & Kus, A. J. 2000, *A&AS*, 143, 269
 Tafalla, M., Myers, P. C., Caselli, P., Walmsley, C. M., & Comito, C. 2002, *ApJ*, 569, 815
 van der Walt, D. J., Gaylard, M. J., & MacLeod, G. C. 1995, *A&AS*, 110, 81
 Weingartner, J. C., & Draine, B. T. 2001, *ApJ*, 548, 296
 Williams, S. J., Fuller, G. A., & Sridharan, T. K. 2004, *A&A*, 417, 115
 Wood, D. O. S., & Churchwell, E. 1989, *ApJS*, 69, 831
 Zinnecker, H., McCaughrean, M. J., & Wilking, B. A. 1993, in *Protostars and Planets III* (Tucson: Univ. Arizona Press), 429
 Zoonematkermani, S., Helfand, D. J., Becker, R. H., White, R. L., & Perley, R. A. 1990, *ApJS*, 74, 181